

Article

Investigation of the Porosity Gradient in Thickness Direction Formed by Cold Rolling in Porous Aluminum

Jörn Tychsen *  and Joachim Rösler 

Institute for Materials Science, Technische Universität Braunschweig, Langer Kamp 8,
38106 Braunschweig, Germany

* Correspondence: j.tychsen@tu-braunschweig.de; Tel.: +49-531-391-3067

Abstract: To adapt porous material for its application as low noise trailing edge, a special rolling process, using a time-varied rolling gap, was used in previous research to produce a porosity gradient in the direction of rolling. Investigations suggest that a gradient in porosity may also be produced in the thickness direction of the material, i.e., in the rolling gap direction, without using a specialized rolling mill. Such a gradient may help to further increase acoustic efficiency of porous materials. The aim of this study was to analyze the dependency of such a gradient on the rolling parameters, and to clarify which stress components are significantly responsible for an increased near-surface compaction. Experiments using different relative compressed lengths were performed to analyze shear-dominated and friction-dominated rolling. The material was characterized using compression tests, computed tomography and flow resistance measurements. It is shown that the compressed length is an important parameter for adjusting a porosity gradient. Rolling with small values of compressed length during all rolling passes leads to increased compaction of near-surface regions, compared to interior ones. The difference in porosity achieved was up to 15%. Furthermore, the results suggested that a gradient in hydrostatic stress is responsible for the porosity gradient. Validation of the results by FE simulation is forthcoming, but not part of this publication.

Keywords: cold rolling; porous aluminum; pore structure; porosity; computed tomography; gradient; hydrostatic stress; shear stress; flow resistance



Citation: Tychsen, J.; Rösler, J. Investigation of the Porosity Gradient in Thickness Direction Formed by Cold Rolling in Porous Aluminum. *Metals* **2023**, *13*, 681. <https://doi.org/10.3390/met13040681>

Received: 14 February 2023

Revised: 20 March 2023

Accepted: 22 March 2023

Published: 30 March 2023



Copyright: © 2023 by the authors. Licensee MDPI, Basel, Switzerland. This article is an open access article distributed under the terms and conditions of the Creative Commons Attribution (CC BY) license (<https://creativecommons.org/licenses/by/4.0/>).

1. Introduction

When rolling porous material, it was found that compaction may not be constant in thickness direction, depending on the rolling parameters [1]. This effect was investigated, to be understood in detail, by performing experiments and finite element modeling. The results of the experiments are presented in this paper. On the one hand, the results were already meaningful without finite element simulation and, on the other hand, the number of experiments made it desirable to present the results separately. Finite element analysis is to be finalized and published. Reference will then be made to the present publication. In the following introduction, the motivation for the investigations is presented in detail, as the proposed application affected the method and target of the experiments. Subsequently, the working hypothesis is explained and considered in the context of current research.

Flow noise is a major contributor to sound perceived as aircraft noise in the neighborhood of airports [2,3]. Aircraft noise can affect the health of residents [4–6] and so, since traffic density continues to increase and cities are growing such that urban areas are moving closer to airports, reduction of aircraft noise has become an important part of research in aviation. In addition to airflow noise, engines are another major source of noise, particularly during aircraft takeoff. Engine noise has already been reduced, which is why the simultaneous reduction of airflow noise is an important part of current research [2,7–14]. The reduction of airflow noise also plays an important role in wind turbines, in order to increase the acceptance of such turbines in residential areas. So-called serrated patterns are already being successfully used in wind turbines to reduce airflow-generated noise [15].

As part of the finalized CRC880 research project, various materials were investigated to be used as so-called low-noise trailing edges [1,16–18]. The material is not used to dampen sound waves that have already been generated. The material is intended to prevent, or reduce, the generation of sound at the trailing edge [14]. The sound source arises because overflow from suction and pressure sides meet at the trailing edge of an airfoil. In simple terms, porous materials can create a smooth pressure equalization from suction to pressure side all the way to the trailing edge, so that sound generation is reduced at this point. However, by attaching porous materials, a sudden transition is created at the point of attachment, which results in a sound source. Aeroacoustic simulations have shown that a porosity gradient along the overflow direction can significantly improve aeroacoustic behavior [18–20]. The sound source at the trailing edge is mitigated, and a gradient transition from solid airfoil to porous insert can prevent the emergence of a second source.

The fact that the lift coefficient decreases slightly must not be neglected. Additional fuel consumption can be accepted during takeoff and landing cases, since noise reduction justifies the increased consumption. For cruise flight, however, a design solution must be devised to prevent reduction in the lift coefficient. It would be sufficient to prevent an exchange of air from suction and pressure sides. For example, with a thin sheet that covers the porous insert on one side during cruise flight.

Concerning the gradient being favored by aeroacoustic simulations [19] a rolling process was used to set it within the porous material [16,21]. The rolling gap was changed during each rolling pass so that material was rolled in the form of a wedge. The detailed principle of the rolling mill is described in Tychsen et al. [16]. A similar rolling process was first used for non-porous material, by Hauger [22]. The focus of investigations in [16,21] was on setting a flow resistivity gradient required in advance by aeroacoustic simulations. This goes hand in hand with a gradient in porosity. It was shown by Lippitz [1] that, depending on the rolling parameters, a gradient in the thickness direction of the material may arise in addition to the gradient set by the variable rolling gap. This gradient in thickness direction may influence aeroacoustic efficiency of the material, since the flow resistivity is not constant over the thickness. This was taken into account for the fabrication of experimental trailing edges for wind tunnel tests [21].

Initially, the reason for the formation of a gradient in thickness reduction was unknown, as well as whether it may be adjusted in a targeted manner. Understanding the reason for the gradient and the possibility of targeted superimposition of gradients (i.e., gradient in thickness direction and gradient in rolling direction) may improve the production of low-noise trailing edges. The required flow resistivity could be adjusted primarily by densifying near-surface areas, so that porosity in the interior is kept constant. This may allow a similar aeroacoustic effect to be achieved while using less material and, thus, save a considerable amount of weight. It is also conceivable to adapt porous materials in this way for other applications, such as filters, or applications that are to be discovered. Research on the influence of rolling parameters on the gradient has potential to open up new possibilities for the targeted adaptation of porous materials by rolling.

The aim of this study was to show that such a gradient can be targeted and adjusted depending on the rolling parameters. The basic research hypothesis to be investigated here was that the observed porosity gradient in thickness direction is the result of a hydrostatic stress gradient in this direction which, in turn, depends on the relative compressed length l_d/h_m (l_d , the compressed length, h_m mean thickness, of the rolled material). It was found that the physical parameter responsible for the porosity gradient is a gradient in hydrostatic stress. A simple illustration, see Figure 1, based on force flow lines, illustrates the connection between hydrostatic stress gradient and relative compressed length. Two cases are shown in which a specimen (dark gray) is compressed by a stamp (light gray) on the upper and lower sides. If l_d/h_m (l_d is large, as shown in Figure 1b, bulging of the force flow lines on the sides plays a minor role, so that their density and orientation are almost constant over most of the contact length. Consequently, mean stresses are similar throughout the material thickness and so is the reduction in porosity due to plastic deformation under

a negative mean stress. If, on the other hand, the relative compressed length is small (Figure 1a), the bulging of the force flow lines, and their resulting reduction in density in the center of the material, leads to much lower compressive stresses in the center than towards the material surface. Consequently, plastic deformation is initially limited to the surface areas. Due to the negative mean stress, a reduction of the pore volume fraction occurs there while it is still unaltered in the center. Additionally, a volume element close to the surface that is plastically-compressed in the vertical direction attempts to lengthen in the horizontal direction. However, this is hindered by the material in the center that has not yet plastically-deformed. As a result, additional stresses are generated in the horizontal direction which are compressive at the surface and tensile in the center of the material. This shifts the mean stress to more negative or more positive values at the surface or center, respectively, intensifying the hydrostatic stress gradient in the thickness direction. It also decreases or increases the van Mises equivalent stress at the surface or center, respectively, so that, eventually, plastic deformation also sets in at the center of the material. However, as the hydrostatic stress gradient is maintained, the porosity gradient also further evolves. Finally, it should be pointed out that friction between tool and material surface adds to the compressive stresses in the horizontal direction there, i. e. to a hydrostatic stress gradient in the thickness direction.

The two cases represent, in simplified form, the situation during rolling. Depending on the selected roll infeed, it is possible to work with a small compressed length (Figure 1a) or with a large compressed length (Figure 1b).

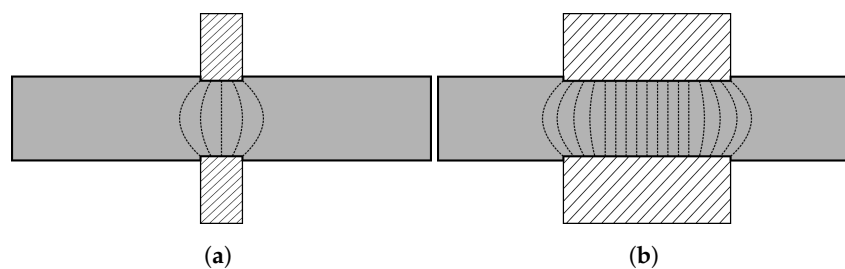


Figure 1. Simplified representation of force flow lines during cold rolling: (a) Small compressed length. (b) High compressed length.

Compressed length is calculated according to Equation (1), using the radius r of the working rolls and the roll infeed Δh_n for each rolling pass (see Equation (2)). The compressed length can be controlled directly by adjusting the roll infeed, by changing the number of passes n until the desired material thickness is reached. Furthermore, the radius of work rolls changes the compressed length. Since roll radius is usually fixed on the machine side, the investigations in this publication focused on the change in infeed Δh_n .

$$l_d = \sqrt{r\Delta h_n - \frac{\Delta h_n^2}{4}} \approx \sqrt{r\Delta h_n} \tag{1}$$

$$\Delta h_n = h_{n-1} - h_n \tag{2}$$

At this point, reference must be made to the flow law for porous metals by Deshpande et al. [23]. The flow equation has the form

$$f(\sigma_{ij}) = \sigma_v(\sigma_{ij}) - \sigma_{krit} = 0 \tag{3}$$

with equivalent stress

$$\sigma_v(\sigma_{ij}) = \frac{\sqrt{\sigma_{vm}^2 + \alpha^2 \sigma_m^2}}{\sqrt{1 + (\alpha/3)^2}} \tag{4}$$

where σ_{vm} is the van Mises equivalent stress and σ_m is the mean stress [23]. The value α describes the spreading of the elliptical flow surface in $\sigma_{vm} - \sigma_m$ -space. Deshpande et al. [23]

showed that associated flow is a reasonable assumption for the porous metals, Alporas and Duocel, they considered. Due to associated flow, the relation

$$\frac{\dot{\epsilon}_m}{\dot{\epsilon}_v} = \frac{\alpha^2}{1 + (\alpha/3)^2} \cdot \frac{\sigma_m}{\sigma_v} \quad (5)$$

for the equivalent volumetric plastic strain rate $\dot{\epsilon}_m$ can be derived, where $\dot{\epsilon}_v$ is the equivalent plastic strain rate and σ_v is the equivalent stress. The Equation (5) shows there is no change in plastic strain due to volume change for pure shear stress states ($\sigma_m = 0 \Rightarrow \dot{\epsilon}_m = 0$). Thus, with the assumptions made, porosity does not change for pure shear stress states.

This leads to the expectation that compaction of porous material during rolling should almost exclusively be based on hydrostatic stress and the working hypothesis mentioned above that a gradient in porosity in the thickness direction is caused by a gradient in the hydrostatic stress in the thickness direction, which may occur in dependence on the relative compressed length.

There are few works dealing with rolling of porous materials, and these usually focus on the modification of functional properties and not on the forming behavior per se (for example [24–26]). Thus, at this point it is necessary to consider studies on non-porous material. Studies on shear strain [27,28] seem to be of particular importance, since these may lead to differences (e.g., grain size distribution [29,30]) in the thickness direction of the material when rolling non-porous material.

Consequently, a conceivable alternative hypothesis is that shear stresses are responsible for a porosity gradient caused by rolling processes in porous materials. In the context of developing high-speed models for real-time simulations of rolling, Seuren et al. [28] were particularly concerned with shear stresses using finite element simulations. They revealed significant the influence of shear stress on rolling behavior. Seuren et al. [28] came to the conclusion that two major domains exist with respect to shear stress. These domains can be partitioned as a function of the relative compressed length l_d/h_m . The definition of the relative compressed length used in Seuren et al. [28] is calculated from the compressed length (Equation (1)) and the mean specimen thickness h_m (Equation (6)). The mean specimen thickness is to be calculated for each rolling step with the thickness of the sample before h_{n-1} and after h_n rolling step number n .

There is a shear-dominated $l_d/h_m \lesssim 1$ domain and a friction-dominated $l_d/h_m \gtrsim 1$ domain [28]. In the shear-dominated domain, shear stresses are caused by path length differences between different material points. The maximum of shear stress is slightly below the material surface (at a depth of 0.7–0.9 relative material thickness). In the friction-dominated domain, shear stress is mainly caused by friction between the rolled material surface and the roll surface. Shear stress increases steadily towards the surface of the rolled stock. The area $0.8 \lesssim l_d/h_m \lesssim 2$ is defined by Seuren et al. [28] as a transition region.

$$h_m = 0.5(h_{n-1} + h_n) \quad (6)$$

The possibility that shear stresses are responsible for a porosity gradient in thickness direction must, therefore, be taken into account, even though this contradicts the material model of Deshpande et al. [23]. Rolling tests performed in this work therefore cover a wide range related to the shear stress domains introduced by Seuren et al. [28].

In this publication it is shown that a porosity gradient in thickness direction can be rolled in a targeted manner. The results suggest that a gradient in hydrostatic stress is the relevant physical parameter responsible for the formation of a porosity gradient. The working hypothesis is that the porosity gradient is dependent on the compressed length because of a hydrostatic stress gradient that forms. This is supported by the results. It is shown that shear stress is most likely not primarily responsible for the evolution of the gradient. FE simulations are to be carried out with the material data obtained to substantiate the results, and will be published in a following publication.

2. Materials and Methods

The aims of the experimental program were the following:

1. to determine the correlation between rolling parameters and the formation of a gradient in porosity in the thickness direction
2. to demonstrate that the gradient can be adjusted by rolling parameters
3. to critically evaluate the following: (i) the working hypothesis that a gradient in hydrostatic stresses is causative for the porosity gradient and (ii) the potential role of shear stress gradients in this respect
4. to provide a database of experimental porosity data for comparison with ongoing FE simulations.

2.1. Material

Porous aluminum from the company “Exxentis”, made of technically pure aluminum (according to Russian standard GOST, A85) with a filter fineness of 80–110 μm , was used for the tests. The pore size of this material ranges from 0.35 mm to 1.00 mm. The openings between the pores, which defines the filter fineness, is 80 μm to 110 μm . The data were taken from the material data sheet sent with the order. The material is produced by casting molten aluminum into a pack of sodium-chloride particles under pressure. This results in an irregular structure with open pores once the sodium-chloride particles are washed out (Figure 2).

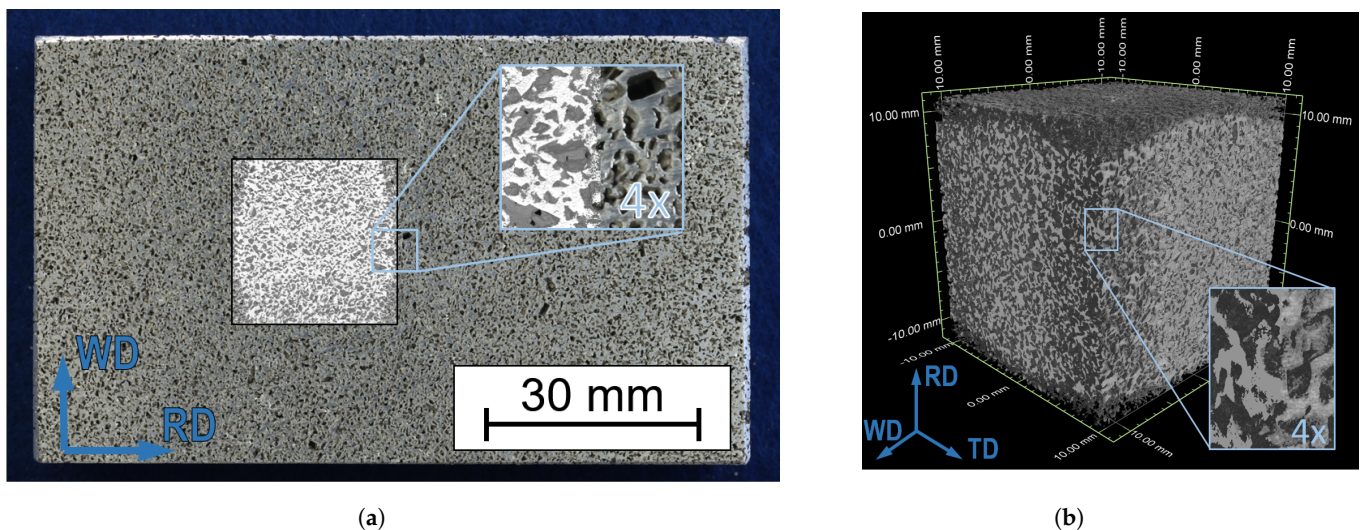


Figure 2. PA80–110 (RD: rolling direction, TD: thickness direction i.e., roll gap direction, WD: width direction i.e., roll width direction): (a) Macro image of a rolling specimen with superimposed area showing the reconstruction of the associated computed tomography scan. (b) three-dimensional CT reconstruction.

The material was used because it showed promising aeroacoustic behavior and good formability by rolling [1,17,18,21,31,32]. The open porosity of up to 60% pore volume fraction allows compaction in a wide range without completely preventing flow through the material (closed porosity). Furthermore, the selected process route (recasting of a placeholder structure and forming by rolling) is well scalable, such that large structures would also be producible.

Material with an initial thickness of 20 mm and material with an initial thickness of 5 mm was used for the tests. The plates were cut from a cast block by the manufacturer and the sodium-chloride was washed out after cutting. In this way, open porosity was ensured on the surfaces, since the pores could not be smeared during cutting.

The material was delivered in two plates of size $500 \times 300 \times 20 \text{ mm}^3$, as well as in several thin plates of size $100 \times 100 \times 5 \text{ mm}^3$. The cutting out of the samples for experiments was done using a band saw, as well as a cutting machine.

Plates of 20 mm thickness were separated into specimens of size $\approx 55 \times 100 \times 20 \text{ mm}^3$. Ten specimens per plate were used for rolling tests. Cylindrical compression test speci-

mens were obtained from one additional specimen per plate using wire electric discharge machining. The small plates were separated in the center using a cutting machine so that one plate was divided into two specimens of size $\approx 49 \times 100 \times 5 \text{ mm}^3$. Due to the small thickness, no compression test specimens could be worked out of these plates. According to the manufacturer, the plates supplied all came from one casting block, so material data determined from the 20 mm thick plates should apply to all specimens.

The sample size was chosen to be as small as possible to achieve high resolution in the computed tomography scanner. However, it was also necessary to ensure that no effects from the edge areas (in relation to the sample edges in the width direction) had an influence on the results in the analyzed area.

2.2. Compression Test

Compression tests were performed according to DIN 50106 [33], following recommendations by Ashby et al. [34] for porous materials. The sample size was 20 mm in diameter and 20 mm, as well as 30 mm in height. For the samples 20 mm and 30 mm in height the direction of height was parallel to the thickness direction TD and rolling direction RD, respectively. Since loading direction during rolling corresponded to the loading direction of the 20 mm specimens, these were particularly relevant for the rolling tests performed. The 30 mm specimens were intended to show that the material behaved homogeneously.

Test speed was strain controlled at 0.002 1/s and changed to 0.00025 1/s for the hysteresis to determine the sample stiffnesses E^* . Preload was set to 10 N. The loading platens were lubricated with a metal-free, ceramic-based lubricating paste to minimize friction. Tests were performed at an ambient temperature of approximately 21 °C.

The results of the compression tests were used to characterize the material. A detailed scientific evaluation will be carried out in the aforementioned future publication, dealing with the FE simulation of the material, which is yet to be published.

2.3. Rolling Tests

The “Bühler Redex” cold rolling mill used operates with a set of work rolls without back-up rolls. The work rolls have a diameter of 200 mm each. The roll width is 200 mm. The maximum roll gap opening is 24 mm. The specimens were rolled at a rolling speed of 5 mm/s with a concentricity of 2 μm . The roll gap was calibrated to 0.000 mm for the tests at a force of 100 kN. Measured rolling force varied, depending on the roll infeed, between 0–40 kN. The orientation of specimens with respect to the roll gap was always identical, and specimens were not rotated.

Rolling parameters were chosen to set a minimum relative compressed length of 0.21 and a maximum relative compressed length of 4.2. In this way, the two shear stress domains explained in the introduction were covered.

Table 1 shows which conditions were investigated. Two series of tests were performed so that two specimens were rolled from each condition given in Table 1. The table is intended to provide a brief overview of the specimens to simplify understanding in the results section. The specimen naming results from specifying the initial thickness, the total relative plate thickness reduction and the total number of rolling passes. In this way, each specimen is uniquely named. Diagrams in the results section can be quickly assigned to the test parameters. For example, a specimen with an initial thickness of 20 mm, which was rolled down to 10 mm in 3 passes, has the name 20-0.50-3.

Table 1. Sample labels according to test parameters with starting thickness $h_0 = 5 \text{ mm} \vee 20 \text{ mm}$.

Total Relative Thickness Reduction	Total Number of Rolling Passes			
	1	3	10	20
ϵ_{total}				
−0.05	h_0 -0.05-1	h_0 -0.05-3	h_0 -0.05-10	-
−0.15	h_0 -0.15-1	h_0 -0.15-3	h_0 -0.15-10	-
−0.50	h_0 -0.50-1	h_0 -0.50-3	h_0 -0.50-10	h_0 -0.50-20

$$\epsilon_{total} = \frac{\Delta h_{total}}{h_0} \quad (7)$$

The specimens were rolled to the resulting thickness with a constant degree of deformation. The degrees of deformation used and, thus, the sheet thickness reduction resulted from the number of rolling steps and the final thickness to be achieved. The degrees of deformation used are given in Table A1. The resulting thickness values in mm were set at the rolling mill control system up to the calculated third decimal place. The thickness of each sample before and after rolling was measured using a digital caliper with a resolution of 0.01 mm and an maximum measurement error of approximately 22 μm , according to DIN 862 [35].

The actual material thickness values are given in Table 2 for samples of the first test series. The initial thickness of each sample was measured and taken into account for rolling. During experiments, targeted thickness values were not hit perfectly, so deviations occurred. Decisive for the evaluation of the experiments was the specimen thickness after each rolling step. With these values the actual compressed length was calculated. Compressed length and the ratio of compressed length to average specimen thickness during each rolling step were relevant for the analysis of the experiments. Table A2 shows the actual values of the sheet thickness after each rolling step for the second series of measurements.

Note that, for sample “ h_0 -0.50-1”, the feed condition was not met. The specimen was introduced into the roll gap at a roll gap height of 21 mm, while the edge area was in the center of the roll gap. The roll gap was reduced to the required thickness. The remaining part of the sample was then rolled to the required thickness in one pass.

The resulting thickness values for each rolling step in mm were set at the rolling mill control system up to the calculated third decimal place, including a corrective value to compensate for elastic rebound and roll gap calibration at 100 kN. The material correction was around 0.07 mm up to 0.13 mm. These values were known from previous rolling tests and required slight adjustment for each rolling pass.

Table 2. Samples thicknesses before and after rolling for the first series of samples.

ϵ_{total}	Total Amount of Rolling Passes	Initial Thickness h_0 and Thickness h_n after Rolling Pass Number n												
		h_0	h_1	h_2	h_3	h_4	h_5	h_6	h_7	h_8	h_9	h_{10}	[...]	h_{20}
−0.05	1	20.40	19.38	-	-	-	-	-	-	-	-	-	-	-
	3	20.40	20.02	19.71	19.38	-	-	-	-	-	-	-	-	-
	10	20.40	20.24	20.16	20.08	19.98	19.87	19.77	19.69	19.59	19.45	19.39	-	-
	1	4.90	4.65	-	-	-	-	-	-	-	-	-	-	-
	3	4.90	4.81	4.73	4.66	-	-	-	-	-	-	-	-	-
	10	5.00	4.96	4.94	4.91	4.89	4.87	4.85	4.81	4.78	4.77	4.75	-	-
−0.15	1	20.40	17.34	-	-	-	-	-	-	-	-	-	-	-
	3	20.40	19.31	18.31	17.34	-	-	-	-	-	-	-	-	-
	10	20.40	20.03	19.71	19.42	19.10	18.79	18.49	18.20	17.91	17.63	17.34	-	-
	1	5.00	4.23	-	-	-	-	-	-	-	-	-	-	-
	3	5.00	4.73	4.48	4.26	-	-	-	-	-	-	-	-	-
	10	5.00	4.90	4.84	4.75	4.68	4.61	4.54	4.46	4.40	4.32	4.24	-	-
−0.50	1	20.40	9.97	-	-	-	-	-	-	-	-	-	-	-
	3	20.40	16.21	12.87	10.21	-	-	-	-	-	-	-	-	-
	10	20.40	18.99	17.75	16.59	15.46	14.42	13.46	12.55	11.72	10.95	10.20	-	-
	20	20.40	19.69	19.02	18.37	17.76	17.15	16.58	16.01	15.46	14.93	14.44	[...]	10.20
	1	5.00	2.50	-	-	-	-	-	-	-	-	-	-	-
	3	5.00	3.97	3.18	2.50	-	-	-	-	-	-	-	-	-
	10	5.00	4.67	4.36	4.08	3.79	3.53	3.29	3.08	2.87	2.68	2.50	-	-
	20	5.00	4.83	4.67	4.50	4.35	4.21	4.07	3.92	3.79	3.65	3.52	[...]	2.50

2.4. Computed Tomography

A GE nanotom s was used for computed tomography measurements. The detector size was 5 megapixels with a pixel size of 50 $\mu\text{m}/\text{pixel}$. The scanning parameters had to be adjusted depending on the sample thickness and the rolling condition. The X-ray tube settings were optimized for the highest possible resolution for the first series of measurements. The voxel size was 10 $\mu\text{m}/\text{voxel}$ for material of initial thickness of 20 mm. For material of initial thickness 5 mm, the resolution could be set to 8.751 $\mu\text{m}/\text{voxel}$. The X-ray tube was operated at a voltage of 150 kV with 80–90 μA and a copper filter of thickness 0.2–0.02 μm . Over 360°, 2500–3000 images were stored, each composed of 3 exposures at 500–750 ms exposure time. A skip of 0.75–1 s was made between the 3 exposures. In the first series of tests, for the specimens with a rolling pass count of 1 and 3, a CT scan was made after each rolling pass. For the specimens that were rolled with 10 rolling passes, a CT scan was taken after every second rolling pass. For the specimens with 20 rolling passes, a CT scan was made every fourth rolling pass.

In the second series of measurements, a larger area with less resolution was measured. A resolution of 17.5 $\mu\text{m}/\text{voxel}$ was set. The X-ray tube was operated at a voltage of 140 kV with 170 μA and a copper filter of 0.02 μm thickness. Over 360°, 3000 images were stored, each composed of 3 exposures at 500 ms exposure time. A skip of 1 s was made between the 3 exposures. The specimens in the second series of tests were CT scanned only in the initial condition and in the final condition.

In the first test series, areas of $23 \times 23 \times 23 \text{ mm}^3$ (specimen thickness at start 20 mm) and $21 \times 21 \times 21 \text{ mm}^3$ (specimen thickness at start 5 mm) were scanned and reconstructed, respectively. During the second measurement series an area of $40 \times 40 \times 40 \text{ mm}^3$ was analyzed. The evaluation was performed using the “surface identification” and “defect detection” of “VG Studio Max 2.1” software from “Volume Graphics”. Surface detection was performed for each ROI, with the isosurface being placed in the valley between the material peak and the background peak. This isosurface was, in most cases, in good agreement with the isosurface of the ISO50 method. Furthermore, defect detection was performed for each ROI, calculating the porosity P_{ROI} according to Equation (8) using the pore volume $Vol_{por,ROI}$ and the total volume $Vol_{tot,ROI}$. The total volume is the sum of the material volume $Vol_{mat,ROI}$ and the pore volume.

$$P_{ROI} = \frac{Vol_{por,ROI}}{Vol_{tot,ROI}} \cdot 100 = \frac{Vol_{por,ROI}}{Vol_{por,ROI} + Vol_{mat,ROI}} \cdot 100 \quad (8)$$

During rolling, specimens were compressed according to the degree of deformation. At the maximum degree of deformation, broadening ($\approx 2\%$) and elongation ($\approx 20\%$) of the specimens occurred. The center of the computed tomographic measurement remained identical, so a small portion of the initially analyzed volume moved out of the measurement area.

The scanned areas were first divided into 60 regions of interest (ROI) ($h_0 = 20 \text{ mm}$) and 30 ROI ($h_0 = 5 \text{ mm}$), respectively. Three ROI stacks were created with 20 ($h_0 = 20 \text{ mm}$) and with 10 ROI ($h_0 = 5 \text{ mm}$) in sample thickness direction for each. The ROI stacks divided the reconstructed sample in three areas along the rolling direction. This is shown for $h_0 = 20 \text{ mm}$ in Figure 3. The three stacks are called “first stack” “second stack” and “third stack” in the following, as the first stack entered the rolling gap first during rolling experiments. The ROIs were spanned as close as possible to the sample surface. The corners of the outer ROIs were omitted, since measurement artifacts of the CT distort the porosity. The identical ROI template was loaded into each reconstructed volume and centered. The ROIs that protruded from the volumes, due to the decreasing sample thickness, were deleted and replaced by a narrower ROI that also reached as close as possible to the surface. Therefore, the thinner the samples became during rolling, the fewer the number of ROIs. For the second series of measurements, the amount of ROIs for samples with initial thickness of 5 mm increased to ≈ 18 ROIs for each stack.

The position of the ROI center of each ROI within the samples was measured, starting from the surface. In this way, the position of each ROI relative to the current specimen

thickness could be specified. In this way, diagrams could be created which showed positions in thickness direction from 0 to 1 on the abscissa and ROI porosity values P_{ROI} on the ordinate. No standard deviation was given for porosity values as they were calculated from CT measurements with high resolution, specifically for each ROI. The software used provided values to several decimal places, and they were then rounded to two decimal places.

For individual ROIs, a porosity difference found in the initial state could be tracked well to higher forming degrees. Combining the values for the different ROI stacks would, thus, distort the results, as porosity differences in the initial state between ROIs may exceed compaction during rolling. With different initial porosities, a mean value with a high associated standard deviation would result. Therefore, a separate plot was given for each ROI stack.

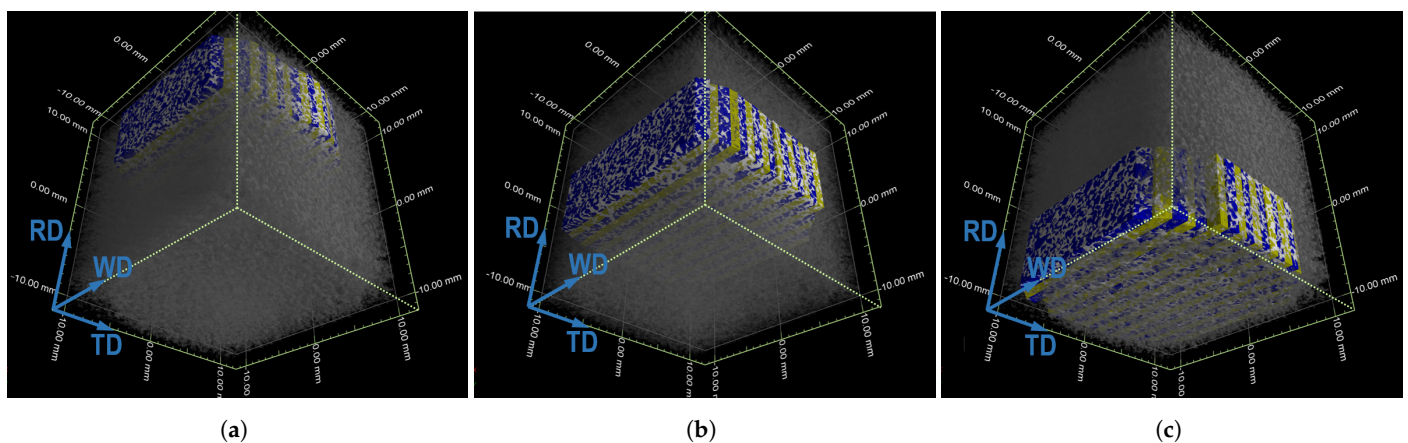


Figure 3. ROI stacks (Pore volume of different ROIs alternately highlighted in color) in sample with $h_0 = 20$ mm (RD: rolling direction, TD: thickness direction i.e., roll gap direction, WD: width direction i.e., roll width direction): (a) First stack. (b) Second stack. (c) Third stack.

2.5. Flow Resistance Measurement

Flow resistance measurements were performed according to DIN 29053 [36] for the first measurement series in the thickness direction. The initial and final rolling conditions were examined. The measurement setup is described in [37]. Since the sample areas differed from the area required in the standard, an area correction was performed, which was designed for the porous aluminum used and proven to be reliable by Blech et al. [37].

The uncertainty in measurement of 14% specified in the standard was not taken into account mathematically in the given values. The measurement of each sample was performed repeatedly, completely removing the sample from the aperture and rotating it in different directions. Thus, measurement uncertainty was taken into account in this way.

Using the flow resistance, it can be shown that not only the porosity of the material changed, but also a physical property that was of great relevance for the originally-planned application of the material in acoustics.

It should be noted that the influence of a gradient of porosity in thickness direction on flow resistance has not yet been researched. Only in Tychsen et al. [21] was the difference in thickness direction taken into account for the production of trailing edges. Usually, a material with a constant flow resistivity over the thickness is desired. Here, a material with changing flow resistivity was produced. In previous publications, flow resistivity was given [16,21,31]. Since the change in values of individual specimens, without offsetting the specimen thickness, was actually relevant at this point, the length-related flow resistance (i.e., flow resistivity) was not used in this publication. The flow resistance determined from the pressure drop is given directly.

3. Results and Discussion

In the following description and discussion of results, particular attention is paid to the porosity data, which must be placed in relation to the working hypothesis. Furthermore, results of the compression tests and the flow resistance measurements are briefly described.

3.1. Compression Test

First of all, it should be emphasized that the results of the compression tests were very similar. This was true both in the comparison of specimens between the first (Figure 4) and the second series of measurements (Figure A1), which were taken from different initial plates, and in the comparison of specimens that had a different height (20 mm or 30 mm). The samples of different heights are shown together within each Figure for each measurement series. The results show that individual samples reflected a reasonable average value of the material. The results of the rolling tests could, therefore, be evaluated without any reservations.

In Figure 4 an elastic region can be seen at the beginning of the stress–strain curves. At the beginning of the plastic region, stress dropped significantly; this was the measuring region of the stiffness using hysteresis. A clear plateau region, as in other open-porous metals, did not follow. Instead, stress increased steadily after hysteresis. A superposition of strain hardening and the beginning of densification in the near-surface areas was a possible cause. It should be noted that compression tests were stopped at around 55% strain. Typically, compression tests of porous materials are continued up to around 90% strain, so that the densification region is much more pronounced than shown here [34]. A slight increase in stress in the plateau region was, therefore, less noticeable. Furthermore, the material used here was less porous, compared to other closed-cell aluminum foams (e.g., Alporas [34]). Strain hardening in the plateau region had a greater impact for the material used here. The behavior shown was in good qualitative agreement with that of sintered 316L steel at 41% porosity, for example [38]. In the plastic region, Doroszko et al. [38] found an increase in stress without a pronounced plateau region, which could be attributed to strain hardening.

The initial stiffness E^* , which is usually not analyzed, since thin struts may deform plastically during initial loading [34], was quite similar for samples of the same thickness: $E_{I-20mm}^* = 4.8 \pm 0.6$ GPa and $E_{II-20mm}^* = 4.6 \pm 0.5$ GPa as well as $E_{I-30mm}^* = 6.6 \pm 1.1$ GPa and $E_{II-30mm}^* = 7.9 \pm 1.3$ GPa. This was also found to be the case for the stiffness using hysteresis: $E_{hys-I-20mm}^* = 24.2 \pm 1.1$ GPa and $E_{hys-II-20mm}^* = 21.8 \pm 0.7$ GPa as well as $E_{hys-I-30mm}^* = 27.2 \pm 0.6$ GPa and $E_{hys-II-30mm}^* = 29.9 \pm 0.7$ GPa (mean values with standard deviation). Stiffness was higher for samples with 30 mm height. However, this could be neglected for the evaluation, since specimens for the rolling tests all corresponded to the orientation and thickness of the 20 mm thick compression test specimens.

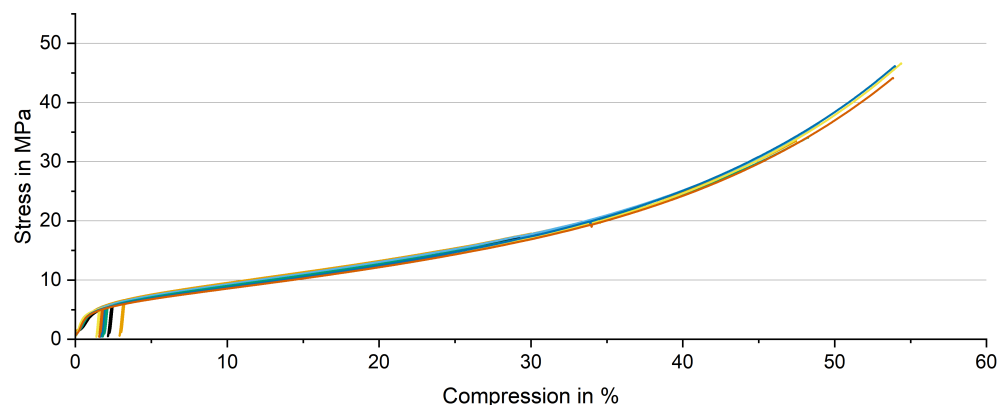


Figure 4. Results of compression tests of PA80–110, first measurement series.

A detailed analysis of the compression tests was not performed at this point. They will be discussed and used to calibrate the material model for the FE simulation of the experiments shown here.

3.2. Rolling Experiments

A selection of measured porosity data from the first series of experiments is shown in the following. The corresponding selection for the second series of measurements, which supports the results found, can be found in the Appendix A, Figures A4–A6, together with

Figure A2 showing the calculated relative compressed length. The other porosity diagrams can be found in the Supplementary Material Figures S1–S20.

In Figure 5 it can be seen that the experimental design to cover a wide range of the relative compressed length was well achieved within the range possible. The calculated relative compressed lengths for each rolling pass of each specimen tested (red crosses for specimens with 20 mm starting thickness and blue crosses for specimens with 5 mm starting thickness) are shown. Next to the crosses, a bar is shown for each specimen, marking the range of the distribution of values for better readability. The largest value was about 4.2 for sample 5-0.50-1. This sample had an initial thickness of ≈ 5 mm and was rolled down to ≈ 2.5 mm in one pass. For sample 20-0.05-10, a value of about 0.21 was obtained for the relative compressed length. This sample had an initial thickness of ≈ 20 mm and was rolled down to 19.40 mm in 10 passes.

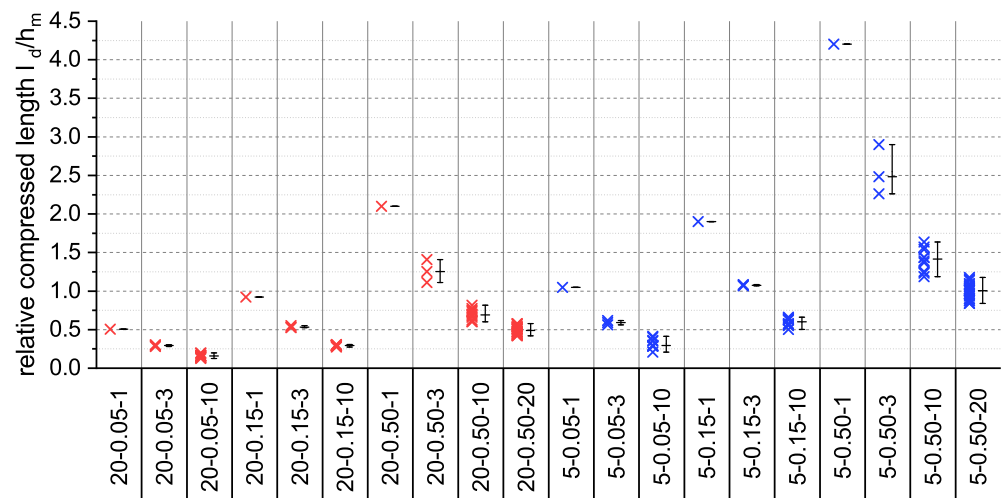


Figure 5. Calculated relative compressed lengths for first series of experiments.

As previously described, there are two domains identified by Seuren et al. [28]. In the shear-dominated domain, located at $l_d/h_m < 1$, the maximum shear stress should be slightly below the surface at about 0.7–0.9 relative material thickness. In the friction-dominated domain, which starts at $l_d/h_m > 1$, shear stresses increase towards the surface to reach their maximum directly at the surfaces of the material.

At this point it is important to note that Seuren et al. [28] analyzed larger specimen dimensions ($h_0 > 40$ mm). In the shear-dominated range, path length differences are decisive for the shear stresses. In the case of the smaller specimens investigated here, it was not possible to set path length differences of a similar magnitude as in the case of large specimens. If this was taken into account in addition to the theoretical classification, the experiments carried out here were certainly in the friction-dominated domain. Whether the shear-dominated domain is actually covered is to be verified in the upcoming FE simulation.

If we now consider two samples which were clearly located in the friction-dominated domain, namely 5-0.50-1 (Figure 6) and 5-0.50-3 (Figure 7), we see an almost constant reduction in porosity for 5-0.50-1 over the entire thickness of the sample.

Assuming that shear stresses are responsible for compaction, maximum shear stresses should be accompanied by maximum compaction. Specimens located in the friction-dominated region should, therefore, be much more compacted directly at the surface than in the interior. This could not be seen for either sample 5-0.50-1 or 5-0.50-3. On the contrary, for 5-0.50-3 a slight increase in porosity towards the surface could be seen. For sample 5-0.50-3 in the center stack, this led to a porosity gradient according to pass No.3, which was similar to a flat-w-shaped curve. The porosity was, therefore, high at the surface, then decreased slightly and increased again slightly towards the mid-section of the material. In the second series, the trend towards higher porosity at the surface was even more

pronounced. This clearly demonstrates that compaction does not increase with the shear stress, thus, ruling out the assumption that porosity gradients may be caused by shear stress gradients (see II-5-0.50-1 Figure A4 and II-5-0.50-3 Figure A5).

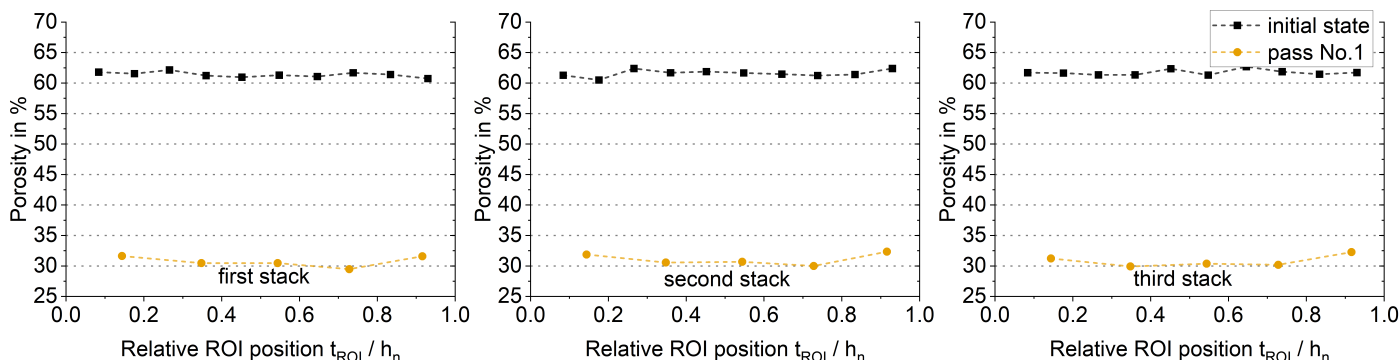


Figure 6. Series I: 5-0.50-1 ($l_d/h_m \approx 4.2$): Porosity change over relative sample depth (0 = upper surface; 0.5 = mid-section of sample; 1 = lower surface) due to rolling for first, second and third stack.

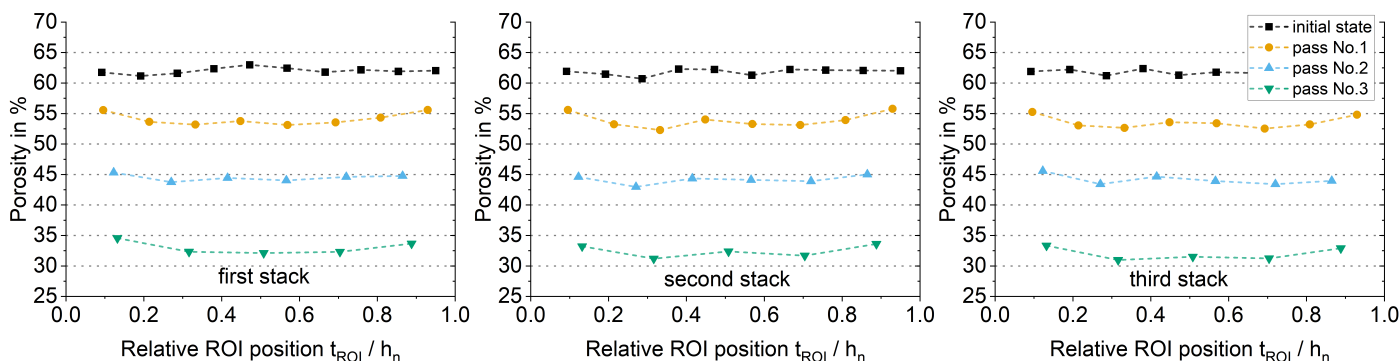


Figure 7. Series I: 5-0.50-3 ($l_d/h_m \approx 2.25 - 2.9$): Porosity change over relative sample depth (0 = upper surface; 0.5 = mid-section of sample; 1 = lower surface) due to rolling for first, second and third stack.

In addition, compaction in the near-surface areas should be greater for samples in the friction-dominated domain than for samples in the shear-dominated domain if shear stresses were relevant. Comparing 5-0.50-1 Figure 6 (friction-dominated) with 20-0.50-20 Figure 8 (shear-dominated) there was no such difference. For 5-0.50-1, the porosity at the surfaces decreased to about 30%. If we now examine sample 20-0.50-20, the porosity there decreased even more to about 25%. In the second series of measurements, the difference seemed to be reversed, so that the sample in the shear-dominated domain (Figure A10) was more compacted at the surface than the sample in the friction-dominated (Figure A4) domain.

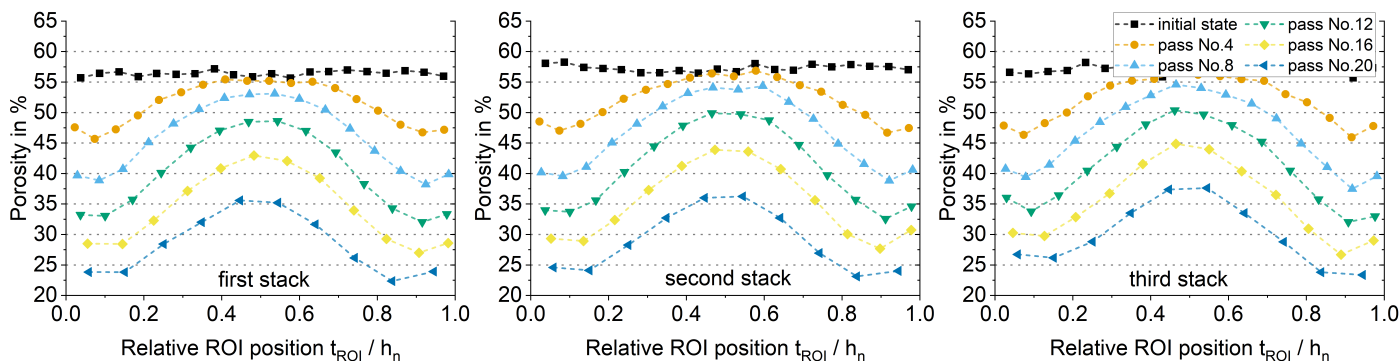


Figure 8. Series I: 20-0.50-20 ($l_d/h_m \approx 0.5$): Porosity change over relative sample depth (0 = upper surface; 0.5 = mid-section of sample; 1 = lower surface) due to rolling for first, second and third stacks.

Note that a slight increase in porosity for some stacks (e.g., 5-0.50-1 Figure 6) can be seen near the surface at the lower surface of the material ($t_{ROI}/h_n = 1$). This can most likely be attributed to the not exactly symmetrical structure of the rolling mill. The bench on which the material was conveyed was positioned just beneath the level of the bottom rolling mill. This slight porosity increase can also be seen in other diagrams, e.g., Figure 9, pass No.20 or in Figure 10 for every stack.

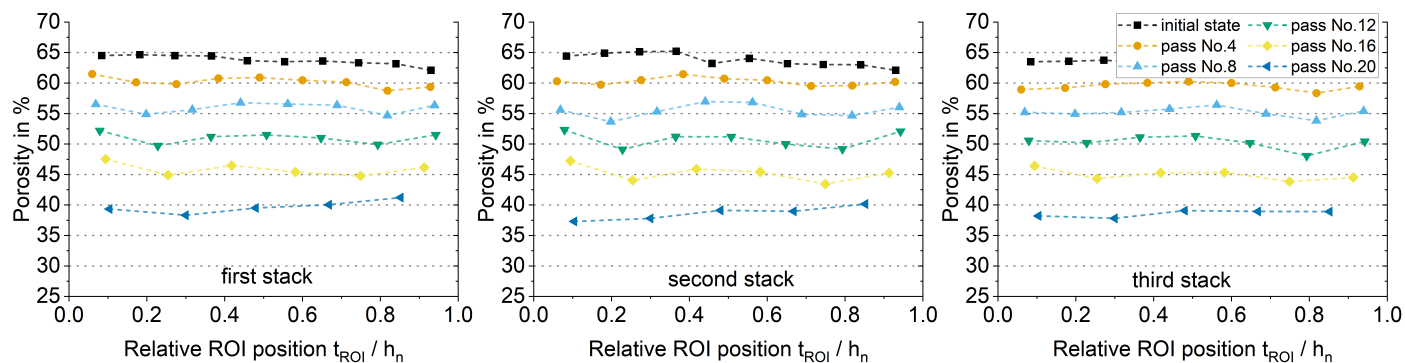


Figure 9. Series I: 5-0.50-20 ($l_d/h_m \approx 0.8 - 1.2$): Porosity change over relative sample depth (0 = upper surface; 0.5 = mid-section of sample; 1 = lower surface) due to rolling for first, second and third stack.

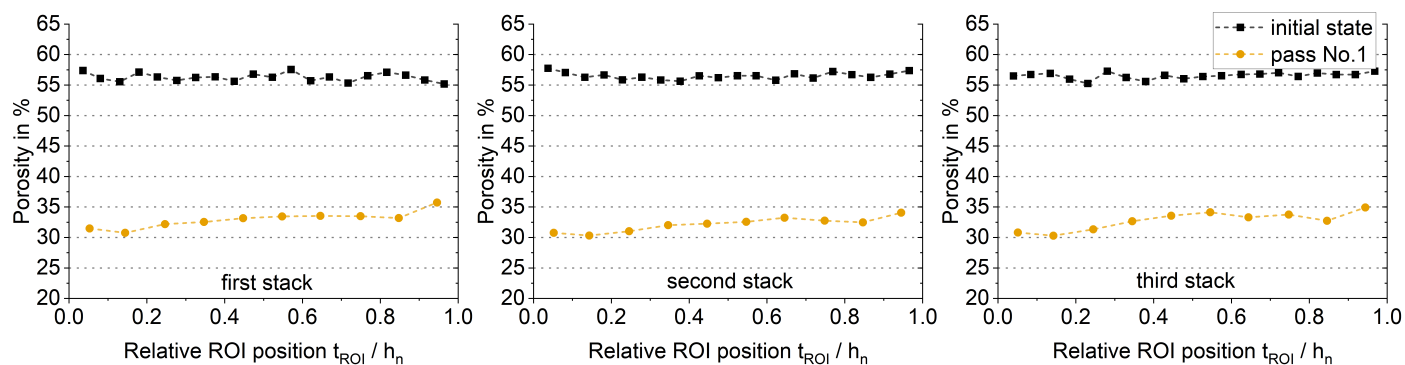


Figure 10. Series I: 20-0.50-1 ($l_d/h_m \approx 2.1$): Porosity change over relative sample depth (0 = upper surface; 0.5 = mid-section of sample; 1 = lower surface) due to rolling for first, second and third stack.

If we now consider specimens which were rolled in the shear-dominated domain, maximum shear stresses were expected to occur 10-30% below the surface, according to Seuren et al. [28]. Thus, a w-shaped porosity curve should result, if shear stresses are responsible for compaction. This should be particularly pronounced for sample 20-0.05-10, which had the lowest value for the relative compressed length (≈ 0.21). Sample 20-0.05-10 is shown in Figure 11. It is clearly visible there was no w-shaped curve in the porosity. Instead, the porosity strongly decreased towards the surface in the outermost 20% of the sample thicknesses while otherwise nearly constant. This also applied to the analogously-rolled sample of the second series of measurements in Figure A12.

However, a w-shaped curve in porosity can be seen in samples 20-0.50-3 (Figure 12) and 20-0.50-10 (Figure 13), and, to a minimal extent, in sample 20-0.50-20 (Figure 8). This also applied to the analogously-rolled samples of the second series of measurements, see Figures A8–A10. Note, that porosity at the surface areas was just 1–2% higher than it was in the most compacted regions. This would support the hypothesis that shear stresses are an important factor in compaction. Albeit, such a w-shaped curve was seen for sample 5-0.50-3 as well (see Figure 7) and was even more pronounced for the analogously-rolled sample of the second measurement series (see Figure A5). These samples, however, were rolled in the friction-domain and should not have had a w-shaped curve in porosity if shear stresses were decisive.

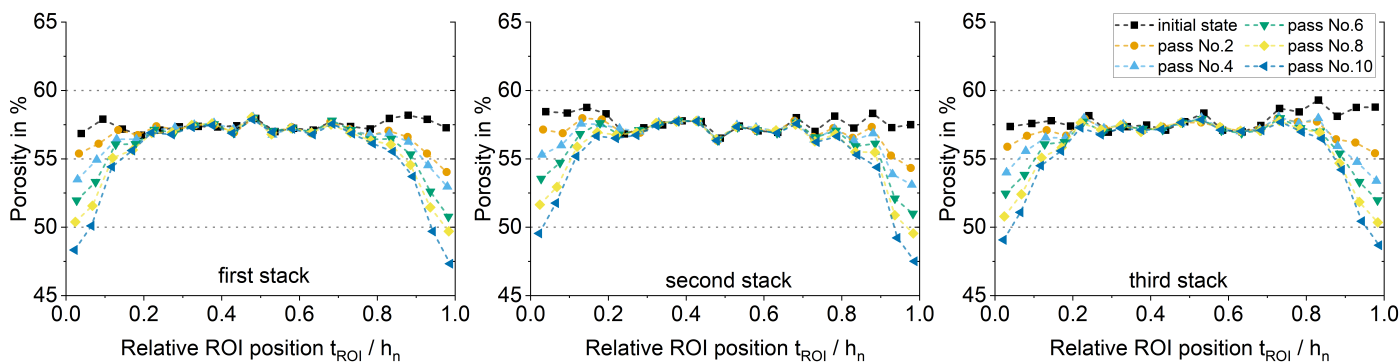


Figure 11. Series I: 20-0.05-10 ($l_d/h_m \approx 0.2$): Porosity change over relative sample depth (0 = upper surface; 0.5 = mid-section of sample; 1 = lower surface) due to rolling for first, second and third stack.

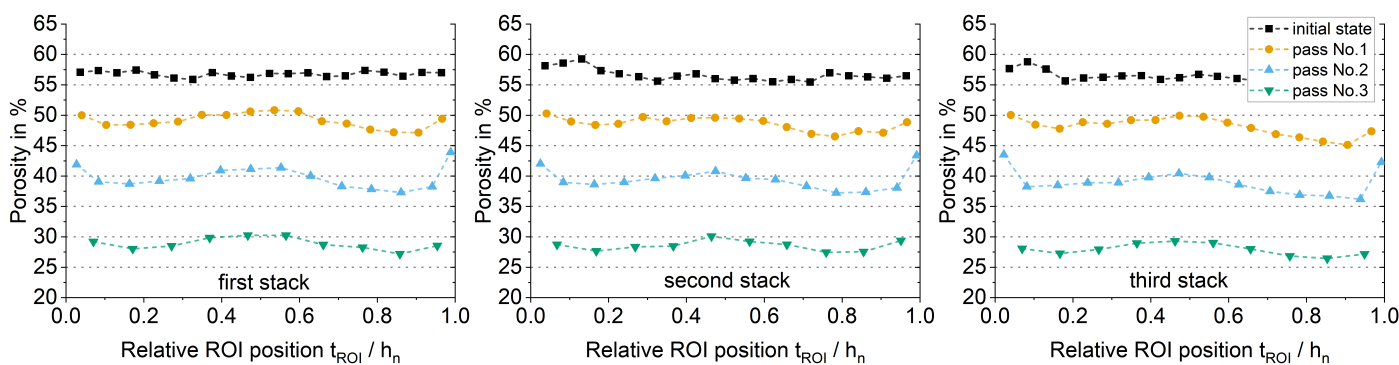


Figure 12. Series I: 20-0.50-3 ($l_d/h_m \approx 1.2 - 1.4$): Porosity change over relative sample depth (0 = upper surface; 0.5 = mid-section of sample; 1 = lower surface) due to rolling for first, second and third stack.

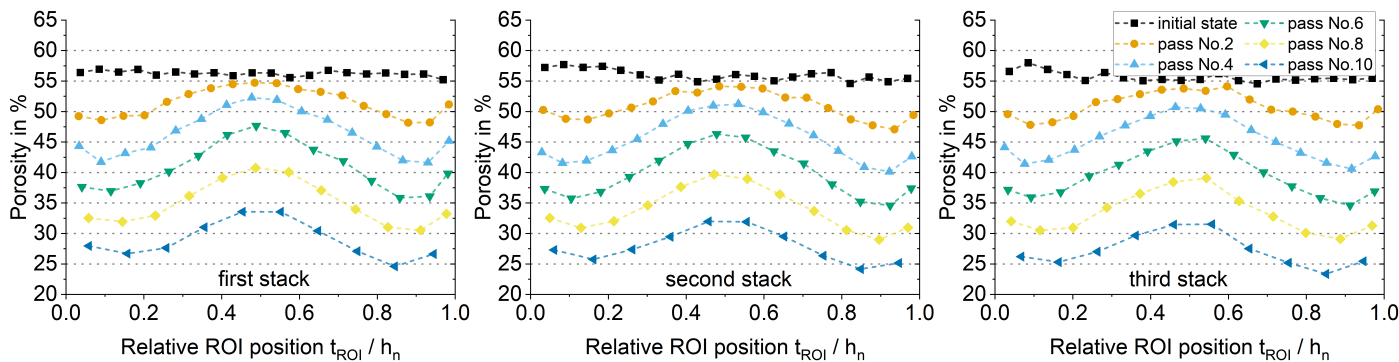


Figure 13. Series I: 20-0.50-10 ($l_d/h_m \approx 0.7 - 0.8$): Porosity change over relative sample depth (0 = upper surface; 0.5 = mid-section of sample; 1 = lower surface) due to rolling for first, second and third stack.

One possibility needing further investigation is that the contact area between the rolled material and the rolling mill, in which elongation and spreading are hindered by friction, also influenced the porosity decrease, which may have led to the w-shape. This could not be investigated in detail at this point as the ROI should have a certain thickness to provide representative results. However, to investigate the aforementioned effect, very thin layers close to the surface need to be analyzed. This work, for which CT scans with higher magnification and/or resolution are necessary, was not part of this study.

The porosity curves obtained must also be evaluated with regard to the working hypothesis of a gradient in the hydrostatic stress component being responsible for the observed porosity gradient. This working hypothesis seemed to be well supported by the experiments. Comparing the specimens with an initial thickness of 20 mm and a final thickness of about 10 mm, the porosity gradient increased as predicted with the number of rolling steps used, i.e., with decreasing relative compressed length. For 20-0.50-1

(Figure 10) almost no difference in porosity from areas close to the surface to the inner part could be seen. For 20-0.50-3 (Figure 12) a minor difference in porosity, of around 2% (absolute value), could be seen. This difference already meant that near-surface areas were around 7% less porous than the inner areas of the material. Sample 20-0.50-10 (Figure 13) showed a recognizable difference, with porosity being approximately 25% less at the surface compared to the porosity of the inner part of the sample (see third stack). This could be observed even more clearly with sample 20-0.50-20 (Figure 8), after 16 rolling passes, where the difference in porosity in thickness direction was around 15% (absolute value) porosity for all stacks, which resulted in an almost 35% less porous surface compared to the inner part of the material.

These results were in line with our expectations, as outlined in Section 1 in conjunction with Figure 1. As l_d/h_m decreased, the gradient in hydrostatic stress from center to surface increased with the hydrostatic stress being more negative at the surface than in the center. Consequently, compaction of the areas close to the surface became more pronounced relative to the center with decreasing l_d/h_m . In the case of sample 20-0.50-20 (Figure 8) it seems that the yield surface was not even reached in the center during the first four passes so that no compaction took place there initially. With further passes, compaction of the center commenced and the porosity gradient appeared to increase in the first eight to twelve rolling passes. Taking the maximum porosity values at the center p_c and the average of the minimum measured ones close to the surfaces \bar{p}_s obtained for the second stack, the porosity gradients $(p_{c,n} - \bar{p}_{s,n})/(h_n/2)$ after n passes were approximately 1.12%/mm, 1.96%/mm and 2.49%/mm after 4, 8 and 12 passes, respectively. However, after 16 passes $(p_{c,16} - \bar{p}_{s,16})/(h_{16}/2) = 2.66\%/mm$ increased very little and after 20 passes it even diminished to 2.47%/mm. On first sight, this seems to be contradictory to our working hypothesis, as one might expect an ever increasing porosity gradient due to a persistent gradient in hydrostatic stress. However, considerable hardening took place on compression, compare with Figure 4, retarding further plastic deformation and compaction of the more compacted region relative to the less compacted one. This set a limit to the maximal achievable porosity gradient. It was obtained after a specific number of passes, depending on rolling parameters and material properties. In the case of sample 20-0.50-20 the highest gradient was achieved after about 12 passes. While much of the hardening was due to compaction, work hardening also played a role. Thus, it is reasonable to assume that the gradient could be further increased if annealing was carried out between rolling steps.

Figure 14a,b show cross sections of the above-described specimen 20-0.50-20 across a sample section in the rolling direction and rolling width plane (RD-WD). It can be seen that the porosity varied significantly after the 16th rolling step between the areas near the surface (Figure 14a) and the mid-area of the specimen (Figure 14b). This can also be seen in Figure 14c, which shows the specimen cut in RD and thickness direction (TD). A strong densification of the material can be seen on both surfaces, which decreased towards the center of the sample. The initial state of the specimen is shown in Figure 14d, where only one half of the cross-section is shown due to space limitations. Porosity was higher compared to the rolled material, as well as being constantly distributed over the entire area of the specimen.

If these results were compared with specimens that had a much lower overall degree of deformation, the effect of localized compaction became even more apparent. Comparing 20-0.05-1 (Figure 15) and 20-0.05-10 (Figure 11) one can see that compaction did not seem to have penetrated into the interior of either sample. Apparently, in both cases, the stresses per pass were too low for the material at the center to reach the yield surface. At 20-0.05-1, it can be seen that no significant compaction took place in a range from 0.4 to 0.6. In the case of 20-0.05-10, this range was approximately between 0.3 and 0.7, which was also reflected in the fact that the porosity gradient of this specimen was much more pronounced. Furthermore, it can be seen that the gradient increased more in the first rolling steps at 20-0.05-10 than during the last rolling steps. This can be clearly seen on the surfaces, i.e., at $t_{ROI}/h_0 = 0$ or 1. Comparing the initial state (black curve)

with the curve after the second rolling step (orange curve), the porosity at the surface changed by about 2.5%. From the eighth to the tenth rolling step (yellow to dark blue curve), the porosity in this area only changed by an average of 1%.

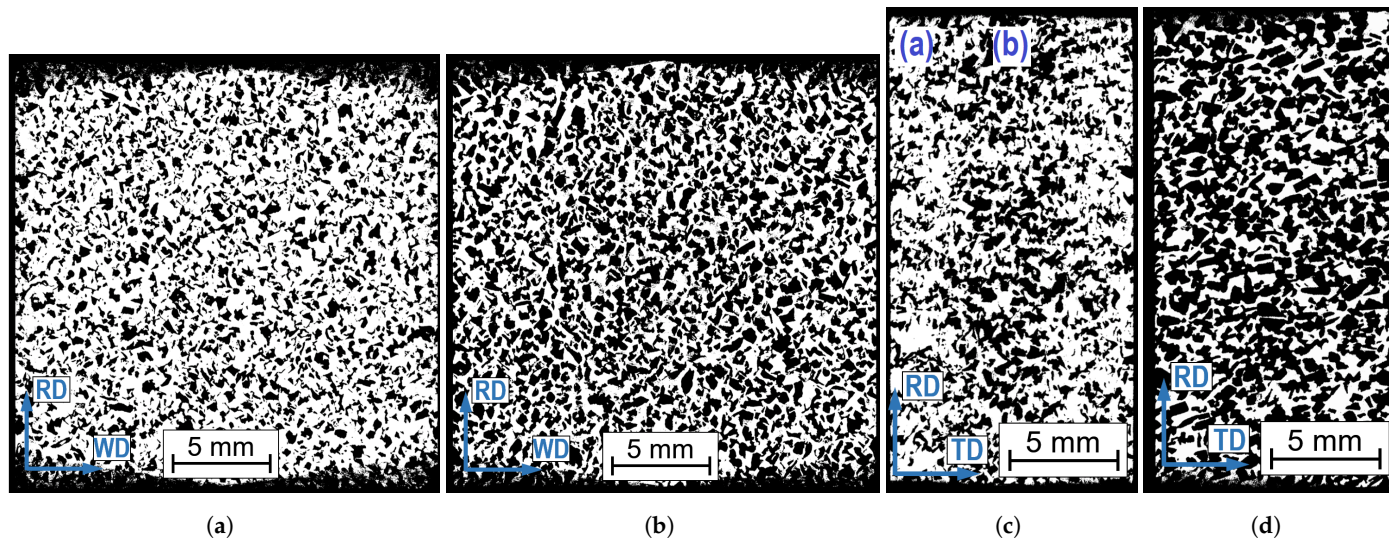


Figure 14. Cross Sections of reconstructed volumes from CT Scans for sample 20-0.50-20 (RD: rolling direction, TD: thickness direction i.e., roll gap direction, WD: width direction i.e., roll width direction, white: material, black: pores): (a) RD-WD at $t_{ROI}/h_n = 0.1$ after pass No. 16. (b) RD-WD $t_{ROI}/h_n = 0.5$ after pass No. 16. (c) RD-TD $t_{ROI}/h_n = 0$ to 1 after pass No. 16. (d) RD-TD $t_{ROI}/h_n = 0$ to 0.5 at initial state.

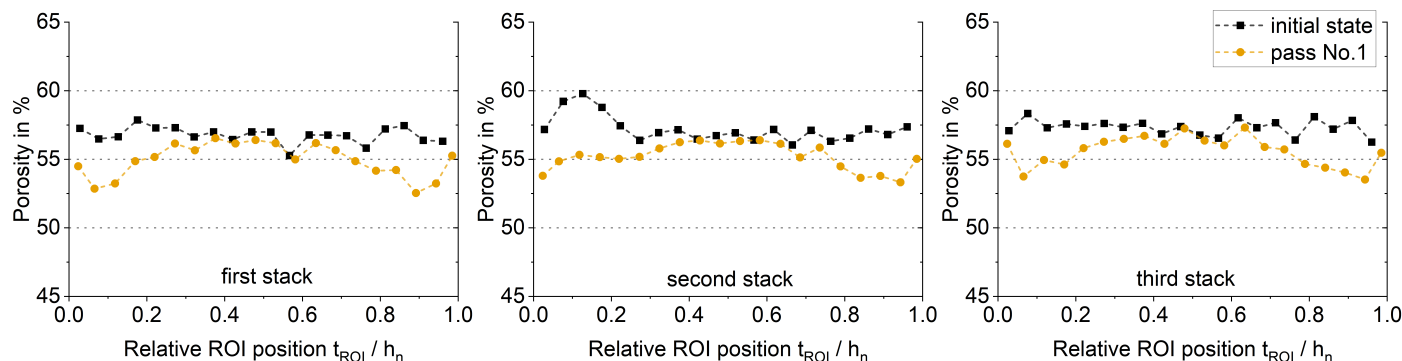


Figure 15. Series I: 20-0.05-1 ($l_d/h_m \approx 0.5$): Porosity change over relative sample depth (0 = upper surface; 0.5 = mid-section of sample; 1 = lower surface) due to rolling for first, second and third stack.

It should be noted that the porosity gradient was much less pronounced for material with an initial thickness of 5 mm. In the case of a rather large relative compressed length, compare with Figure 9 (5-0.50-20), compaction was similar throughout the thickness of the sample, as expected. Only in the third stack of sample 5-0.50-20 could a slight w-shape of the porosity curve be seen. As l_d/h_m decreased, compare with Figures 16 and A3, the w-shape became more pronounced. The cause for this shape evolution needs further evaluation by FE-analysis. Our current interpretation is that a gradient in the hydrostatic stress again evolved as l_d/h_m decreased. This led to a corresponding porosity gradient, as shown by the convex part of the w-shaped curve. However, contact forces between sample and roller hindered plastic deformation and compaction at the sample surface, thus causing the concave part of the w-shaped curve. This effect was more relevant for the material with 5 mm thickness, even though a slight w-shape could also be found in the 20 mm thick samples, as mentioned.

All the results supported the working hypothesis that a gradient in hydrostatic stress significantly affects compaction. As described before, the experiments carried out here were certainly in the friction-dominated domain. The porosity change that would be expected for experiments within this domain, if shear stress is responsible for compaction, was not found. The results of porosity measurements shown here confirmed the working hypothesis. Nevertheless, the results are to be verified with FE simulation of the actual stress state in the rolling gap. Particular attention must be paid not only to the evolution of the hydrostatic stress, but also to the plastic equivalent strain as a function of relative sheet thickness, as in Seuren et al. [28]. In particular, attention must be paid to precisely assigning the different test conditions to the two domains mentioned with respect to shear stress.

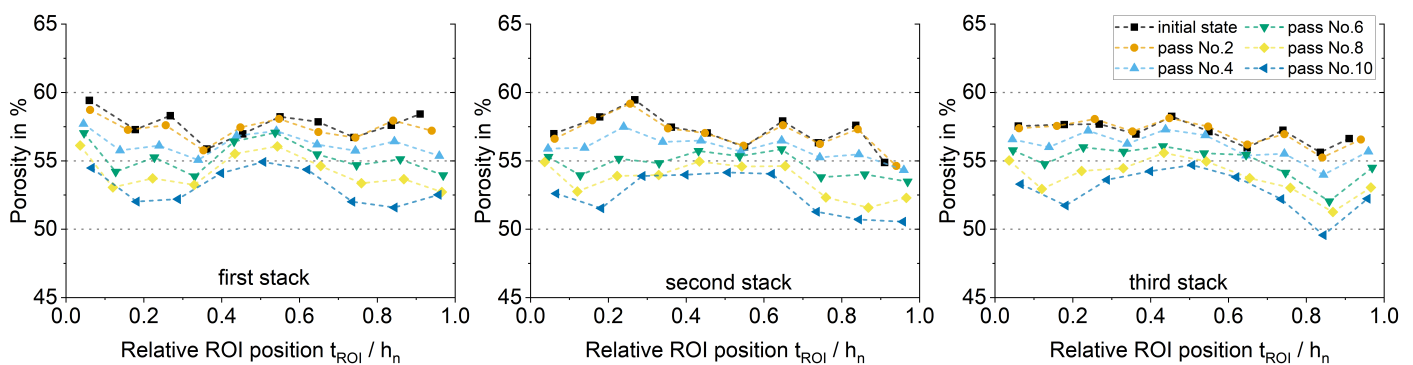


Figure 16. Series I: 5-0.15-10 ($l_d/h_m \approx 0.5 - 0.75$): Porosity change over relative sample depth (0 = upper surface; 0.5 = mid-section of sample; 1 = lower surface) due to rolling for first, second and third stack.

3.3. Flow Resistance Measurements

Based on the flow resistance measurements, it can be shown that change in porosity, due to gradient, affects the physical properties of the material. It must be taken into account that the flow resistance is determined on the assumption of a homogeneous material. A plate with very thin, dense regions close to its surface, but an open core, can have the same total flow resistance as a plate with less dense, but slightly thicker, regions close to its surfaces.

This applies, of course, to the measurements carried out here. In the diagrams of Figure 17 for samples with 20 mm initial thickness and Figure 18 for samples with 5 mm initial thickness, flow resistances of the various samples before and after rolling were plotted. The mean value is given with error bars indicating the standard deviation.

It can be observed rather clearly that all rolled specimens (black) had a higher flow resistance than the unrolled ones (red). For the specimens with 20 mm initial thickness, it was also evident that the flow resistance increased to a greater extent when the resulting thickness was set in many small rolling steps instead of one large one. i.e., when the porosity gradient increased. This was especially true for specimens 20-0.05 and 20-0.15. For the specimens with a sheet thickness reduction of 50%, this effect was only evident when comparing the specimen rolled in one rolling step to the rest. The specimens rolled by 50% with 3, 10 and 20 rolling steps showed no distinctive differences in flow resistance increase.

The specimens with an initial thickness of 5 mm did not show a significant overall increase associated with an increase in rolling steps. On the contrary, the flow resistance for the specimens rolled to 50% thickness increased less the more rolling steps were used.

The results were consistent with the porosity evaluation, in that, for the 20-0.05 and 20-0.15 specimens a significant difference in gradient was found as a function of the number of rolling passes. For the 20-0.50 specimens it was shown that above a certain number of rolling passes the gradient did not increase further. Taking this into account, however, 20-0.50-3 to 20-0.50-10 would have been expected to show an increase in flow resistance. Furthermore, no strong gradient could be set for the thin specimens, so that the differences between specimens rolled in many small steps and specimens rolled in one step were small.

What cannot be explained at this stage is the decrease in the increase in flow resistance with an increase in the number of rolling passes for the 5-0.50 specimens.

The measurements show that the influence of a porosity gradient can be used in a targeted manner to influence flow resistance. It is imaginable to take advantage of this gradient by further enhancing it through annealing, thus obtaining a material with a highly compacted surface, but a highly porous core.

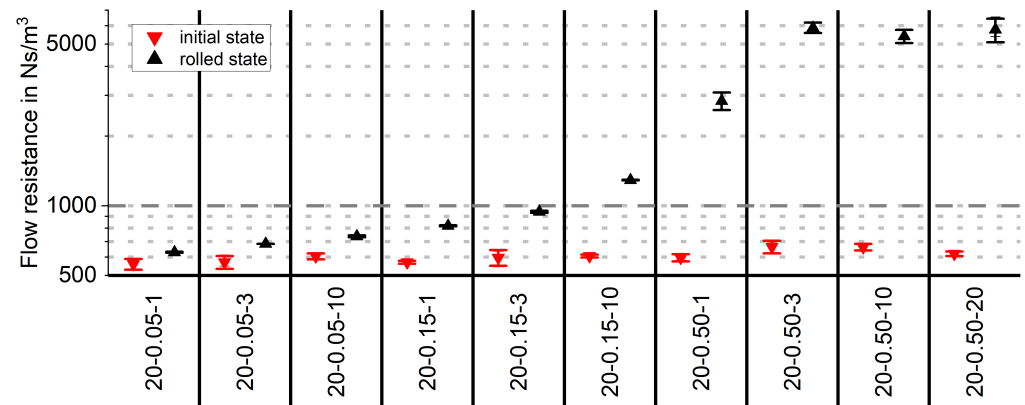


Figure 17. Flow resistance (mean value with standard deviation) for samples with 20 mm initial thickness.

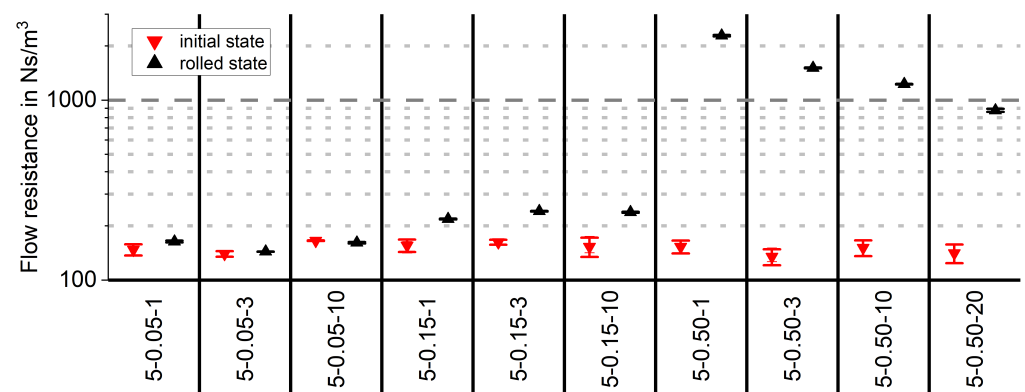


Figure 18. Flow resistance (mean value with standard deviation) for samples with 5 mm initial thickness.

4. Conclusions

During rolling of porous aluminum, a porosity gradient in thickness direction was revealed, which was investigated in this study. The working hypothesis for the development of the porosity gradient is based on the assumption that the hydrostatic stress component is primarily responsible for compaction of porous materials. This premise is the assumption of the material model of Deshpande et al. [23]. The working hypothesis for this study was that by adjusting compressed length using the rolling parameters, a gradient in thickness direction can be set in the hydrostatic stress component, so that a gradient in compaction occurs.

High shear stresses occur during rolling near the surfaces of rolled material. Seuren et al. [28] showed that strain inhomogeneity in non-porous material occurs in dependence on the rolling parameters, as a result of shear stresses. The distribution of shear stresses was investigated and two domains were identified. The friction-dominated domain at $l_d/h_m > 1$ and the shear-dominated domain at $l_d/h_m < 1$.

Based on inhomogeneous strain distribution, one could conclude that a gradient in shear stresses could also influence, or significantly determine, compaction of porous material. This is a contradictory hypothesis to the aforementioned working hypothesis.

A series of rolling tests was carried out, covering a wide range with respect to the stress domains found by Seuren et al. [28]. The experiments were designed to roll samples in both the shear-dominated and friction-dominated domains. Furthermore, experiments were chosen such that, based on the working hypothesis, a strong gradient in porosity was to be expected. An influence of shear stress could not be proven, since the shape of porosity gradients did not fit the shape of maximum shear stress according to Seuren et al. [28]. This applied to specimens rolled in the friction-dominated domain, as well as specimens rolled in the shear-dominated domain. Therefore, though reaching the shear-dominated domain remains to be verified, it can be concluded that the working hypothesis is valid. The shape of the porosity gradient was shown to be dependent on the compressed length. Since a gradient in hydrostatic stress should depend on the compressed length, the results suggest that the relevant physical parameter for the formation of the porosity gradient is a gradient in hydrostatic stress.

The porosity gradient could be adjusted in a targeted manner. It can be maximized by minimizing the compressed length. The results suggest that the extent of the gradient is limited by hardening, resulting from compaction and work hardening. The flow resistance could also be adjusted. The validity of these measurements is limited due to the measurement setup, in which a specimen was measured as a whole.

Further investigations must be carried out by using FE simulation to prove that the assumed stress domains have actually been set. In addition, a gradient in the hydrostatic stress must be verified, which corresponds to the porosity gradient determined here. Furthermore, it should be verified by appropriate experiments whether the gradient can be further enhanced by annealing. With regard to the flow resistances, further measurements should be carried out in order to clarify the behavior shown.

Supplementary Materials: The following supporting information can be downloaded at: <https://www.mdpi.com/article/10.3390/met13040681/s1>, Figure S1: Series I: Porosity of 5-0.05-1 ($l_d/h_m \approx 1.05$); Figure S2: Series I: Porosity of 5-0.05-3 ($l_d/h_m \approx 0.56 - 0.62$); Figure S3: Series I: Porosity of 5-0.05-10 ($l_d/h_m \approx 0.20 - 0.41$); Figure S4: Series I: Porosity of 5-0.15-1 ($l_d/h_m \approx 1.90$); Figure S5: Series I: Porosity of 5-0.15-3 ($l_d/h_m \approx 1.07 - 1.09$); Figure S6: Series I: Porosity of 5-0.50-10 ($l_d/h_m \approx 1.19 - 1.64$); Figure S7: Series I: Porosity of 20-0.05-3 ($l_d/h_m \approx 0.28 - 0.30$); Figure S8: Series I: Porosity of 20-0.15-1 ($l_d/h_m \approx 0.92$); Figure S9: Series I: Porosity of 20-0.15-3 ($l_d/h_m \approx 0.53 - 0.55$); Figure S10: Series II: Porosity of 20-0.15-10 ($l_d/h_m \approx 0.28 - 0.31$); Figure S11: Series II: Porosity of 5-0.05-1 ($l_d/h_m \approx 1.03$); Figure S12: Series II: Porosity of 5-0.05-3 ($l_d/h_m \approx 0.57 - 0.62$); Figure S13: Series II: Porosity of 5-0.05-10 ($l_d/h_m \approx 0.20 - 0.45$); Figure S14: Series II: Porosity of 5-0.15-1 ($l_d/h_m \approx 1.87$); Figure S15: Series II: Porosity of 5-0.15-3 ($l_d/h_m \approx 1.04 - 1.15$); Figure S16: Series II: Porosity of 5-0.50-10 ($l_d/h_m \approx 1.17 - 1.64$); Figure S17: Series II: Porosity of 20-0.05-3 ($l_d/h_m \approx 0.25 - 0.33$); Figure S18: Series II: Porosity of 20-0.15-1 ($l_d/h_m \approx 0.93$); Figure S19: Series II: Porosity of 20-0.15-3 ($l_d/h_m \approx 0.52 - 0.55$); Figure S20: Series II: Porosity of 20-0.15-10 ($l_d/h_m \approx 0.28 - 0.31$).

Author Contributions: Conceptualization, J.R. and J.T.; methodology, J.R. and J.T.; validation, J.R. and J.T.; formal analysis, J.R. and J.T.; investigation, J.T.; resources, J.T.; data curation, J.T.; writing—original draft preparation, J.T.; writing—review and editing, J.R. and J.T.; visualization, J.R. and J.T.; supervision, J.R.; project administration, J.R. and J.T.; funding acquisition, J.R. All authors have read and agreed to the published version of the manuscript.

Funding: This research was funded by Deutsche Forschungsgemeinschaft (DFG) grant number 461192918. We acknowledge support by the Open Access Publication Funds of Technische Universität Braunschweig.

Institutional Review Board Statement: Not applicable.

Informed Consent Statement: Not applicable.

Data Availability Statement: The data presented in this study are available in this article and the Supplementary Materials.

Acknowledgments: We would like to express our sincere thanks to Christopher Blech from the Institute for Acoustics, TU Braunschweig, for performing the flow resistance measurements.

Conflicts of Interest: The authors declare no conflict of interest. The funders had no role in the design of the study; in the collection, analyses, or interpretation of data; in the writing of the manuscript; or in the decision to publish the results.

Abbreviations

The following abbreviations are used in this manuscript:

CRC	Collaborative Research Center
CT	Computed Tomography
FE	Finite Element
RD	Rolling Direction
ROI	Region of Interest
TD	Thickness Direction
WD	Width Direction

Appendix A

Table A1. Total degree of deformation φ_{total} and degree of deformation for each pass of samples with different amounts of total rolling passes 1, 3, 10 and 20.

ϵ_{total}	φ_{total}	φ_1	φ_3	φ_{10}	φ_{20}
−0.05	−0.05129	−0.05129	−0.01710	−0.00513	−0.00256
−0.15	−0.16252	−0.16252	−0.05417	−0.01625	−0.00813
−0.50	−0.69315	−0.69315	−0.23105	−0.06931	−0.03466

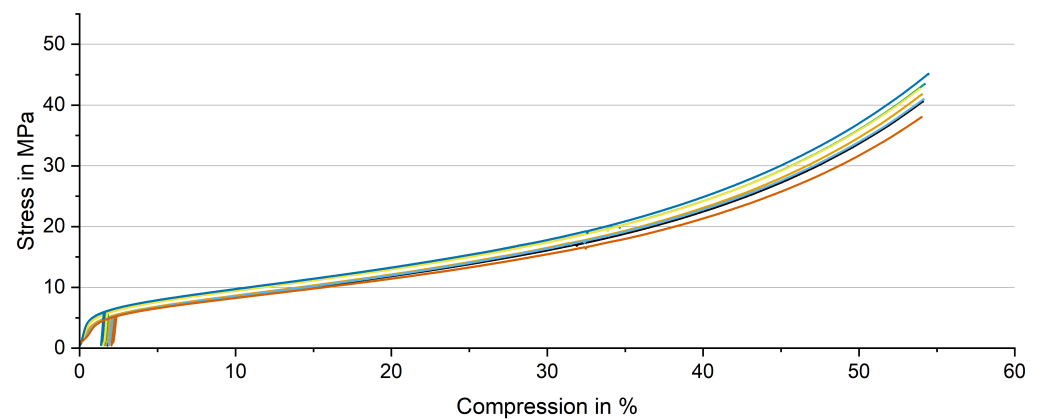


Figure A1. Results of compression tests of PA80-110, second measurement series.

Table A2. Sample thicknesses before and after rolling for the second series of samples.

ϵ_{total}	Total Amount of Rolling Passes	Initial Thickness h_0 and Thickness h_n after Rolling Pass Number n												
		h_0	h_1	h_2	h_3	h_4	h_5	h_6	h_7	h_8	h_9	h_{10}	[...]	h_{20}
−0.05	1	20.10	19.10	-	-	-	-	-	-	-	-	-	-	-
	3	20.10	19.75	19.33	19.10	-	-	-	-	-	-	-	-	-
	10	20.10	20.04	19.88	19.78	19.69	19.58	19.48	19.38	19.33	19.20	19.10	-	-
	1	5.00	4.75	-	-	-	-	-	-	-	-	-	-	-
	3	5.00	4.92	4.83	4.75	-	-	-	-	-	-	-	-	-
	10	5.00	4.95	4.94	4.90	4.89	4.86	4.83	4.80	4.80	4.77	4.74	-	-
−0.15	1	20.20	17.17	-	-	-	-	-	-	-	-	-	-	-
	3	20.20	19.14	18.13	17.17	-	-	-	-	-	-	-	-	-
	10	20.20	19.86	19.54	19.24	18.94	18.61	18.33	18.03	17.74	17.44	17.17	-	-
	1	5.00	4.25	-	-	-	-	-	-	-	-	-	-	-
	3	5.00	4.72	4.49	4.24	-	-	-	-	-	-	-	-	-
	10	5.00	4.93	4.85	4.77	4.69	4.61	4.53	4.47	4.40	4.32	4.25	-	-
−0.50	1	20.20	10.01	-	-	-	-	-	-	-	-	-	-	-
	3	20.10	15.98	12.72	10.07	-	-	-	-	-	-	-	-	-
	10	20.10	18.76	17.50	16.32	15.24	14.22	13.27	12.36	11.56	10.78	10.04	-	-
	20	20.10	19.42	18.76	18.12	17.49	16.90	16.34	15.78	15.25	14.72	14.22	[...]	10.04
	1	5.00	2.52	-	-	-	-	-	-	-	-	-	-	-
	3	5.00	3.98	3.17	2.51	-	-	-	-	-	-	-	-	-
	10	5.00	4.68	4.37	4.09	3.80	3.55	3.31	3.09	2.87	2.68	2.50	-	-
	20	5.00	4.83	4.67	4.51	4.36	4.21	4.06	3.92	3.79	3.66	3.54	[...]	2.51

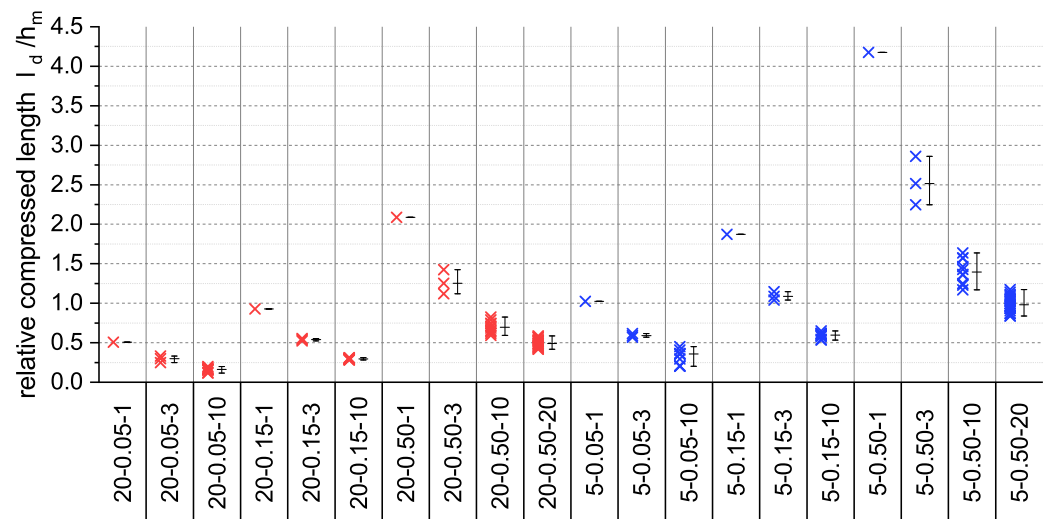


Figure A2. Calculated relative compressed length for second series of experiments.

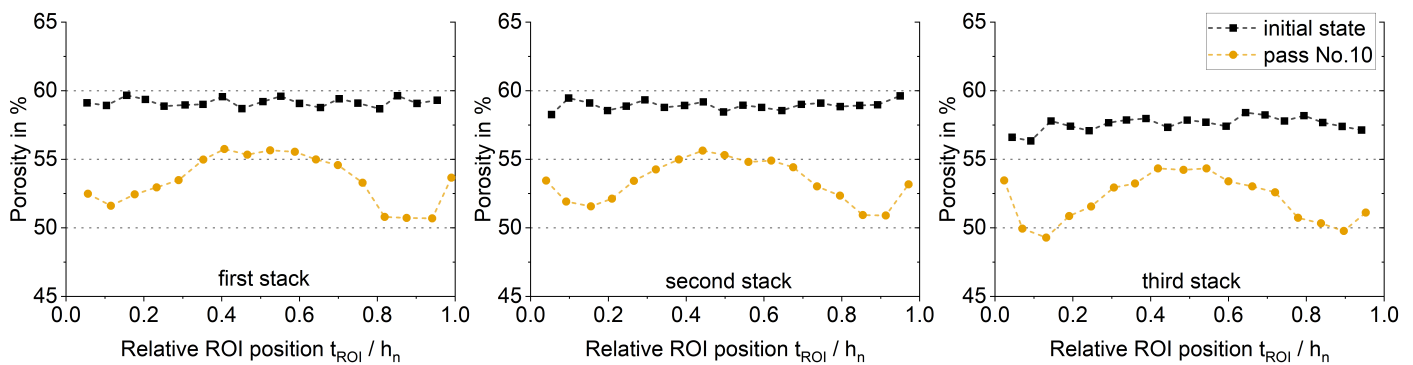


Figure A3. Series II: 5-0.15-10 ($l_d/h_m \approx 0.5 - 0.75$): Porosity change over relative sample depth (0 = upper surface; 0.5 = mid-section of sample; 1 = lower surface) due to rolling for first, second and third stack.

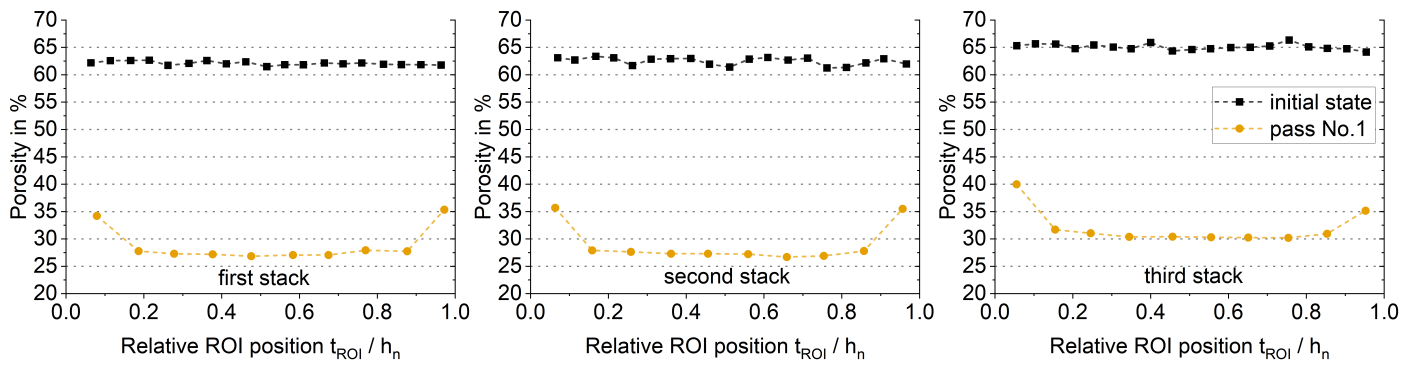


Figure A4. Series II: 5-0.50-1 ($l_d/h_m \approx 4.2$): Porosity change over relative sample depth (0 = upper surface; 0.5 = mid-section of sample; 1 = lower surface) due to rolling for first, second and third stack.

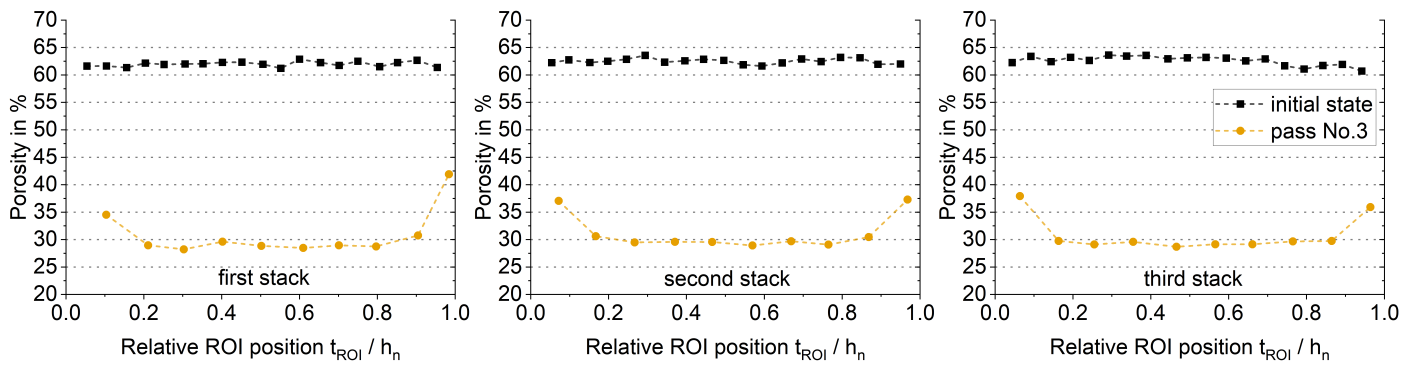


Figure A5. Series II: 5-0.50-3 ($l_d/h_m \approx 2.25 - 2.9$): Porosity change over relative sample depth (0 = upper surface; 0.5 = mid-section of sample; 1 = lower surface) due to rolling for first, second and third stack.

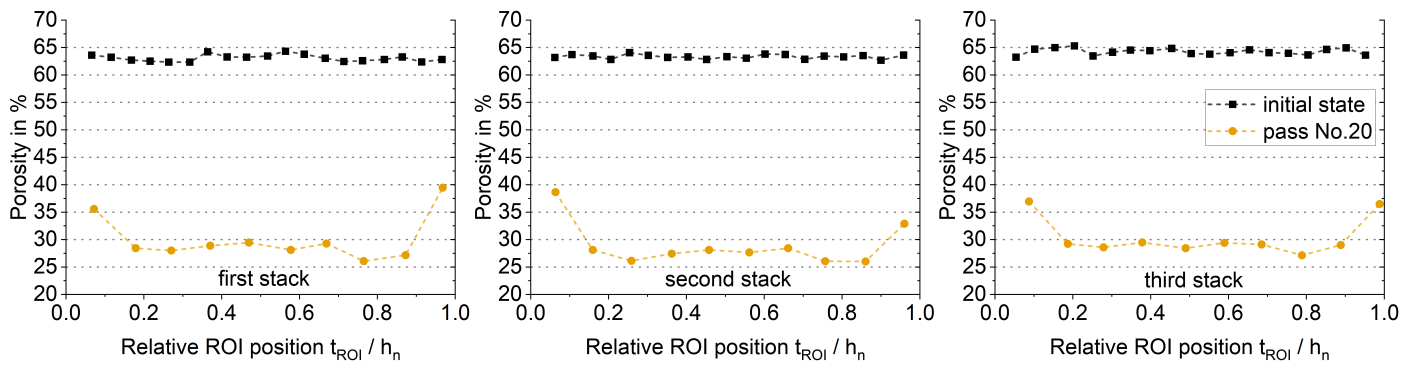


Figure A6. Series II: 5-0.50-20 ($l_d/h_m \approx 0.8 - 1.2$): Porosity change over relative sample depth (0 = upper surface; 0.5 = mid-section of sample; 1 = lower surface) due to rolling for first, second and third stack.

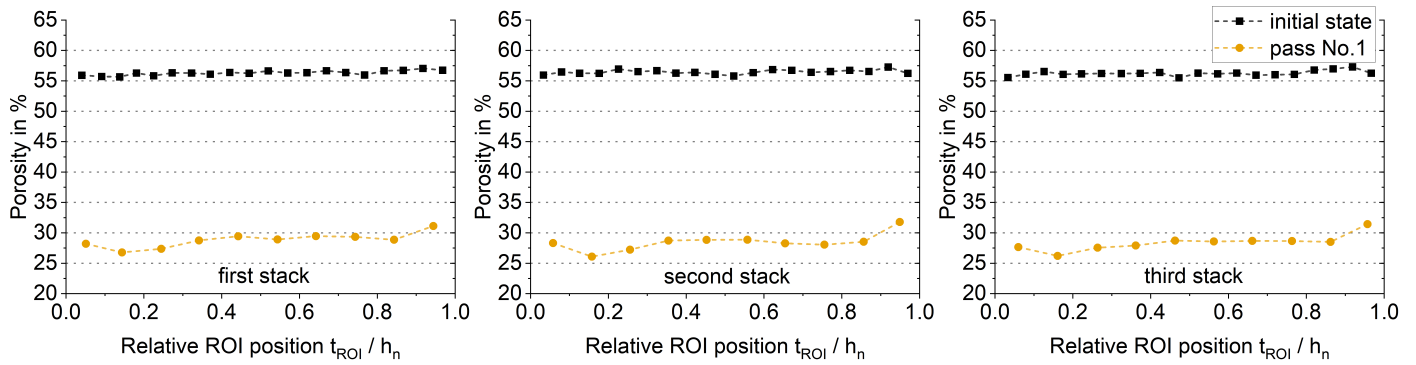


Figure A7. Series II: 20-0.50-1 ($l_d/h_m \approx 2.1$): Porosity change over relative sample depth (0 = upper surface; 0.5 = mid-section of sample; 1 = lower surface) due to rolling for first, second and third stack.

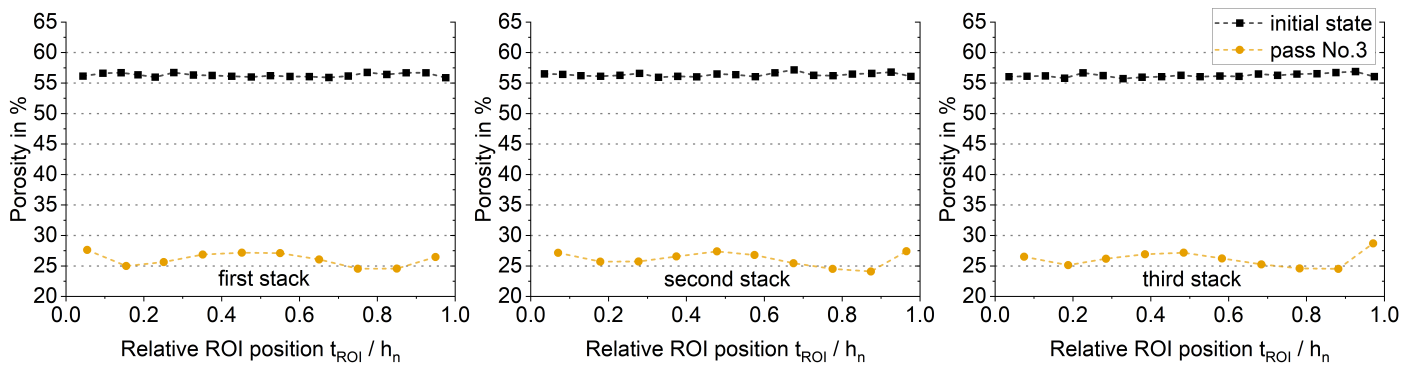


Figure A8. Series II: 20-0.50-3 ($l_d/h_m \approx 1.2 - 1.4$): Porosity change over relative sample depth (0 = upper surface; 0.5 = mid-section of sample; 1 = lower surface) due to rolling for first, second and third stack.

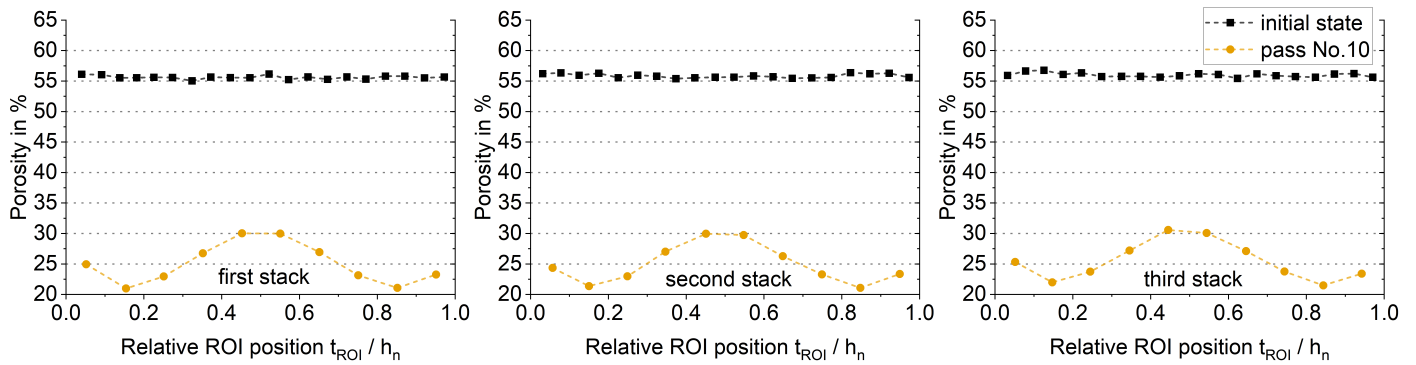


Figure A9. Series II: 20-0.50-10 ($l_d/h_m \approx 0.7 - 0.8$): Porosity change over relative sample depth (0 = upper surface; 0.5 = mid-section of sample; 1 = lower surface) due to rolling for first, second and third stack.

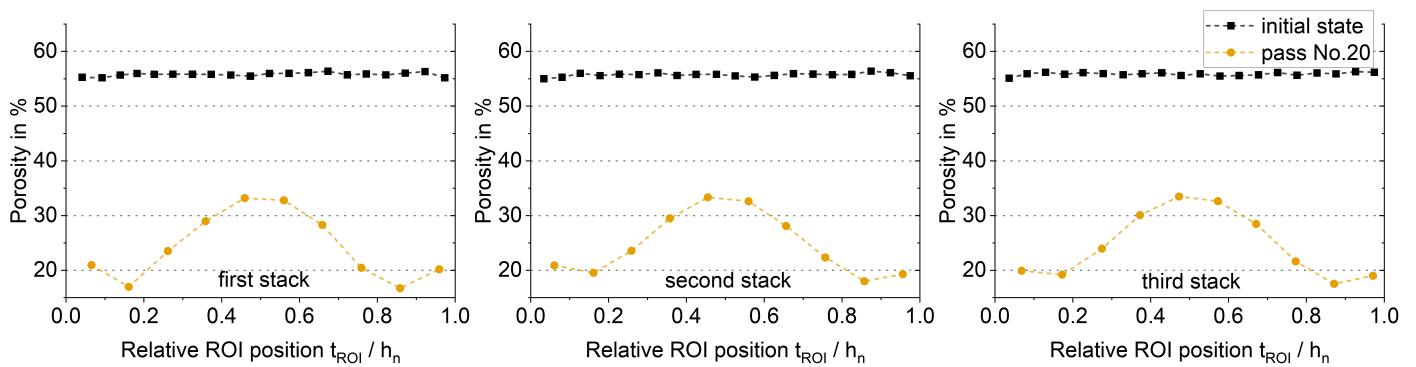


Figure A10. Series II: 20-0.50-20 ($l_d/h_m \approx 0.5$): Porosity change over relative sample depth (0 = upper surface; 0.5 = mid-section of sample; 1 = lower surface) due to rolling for first, second and third stack.

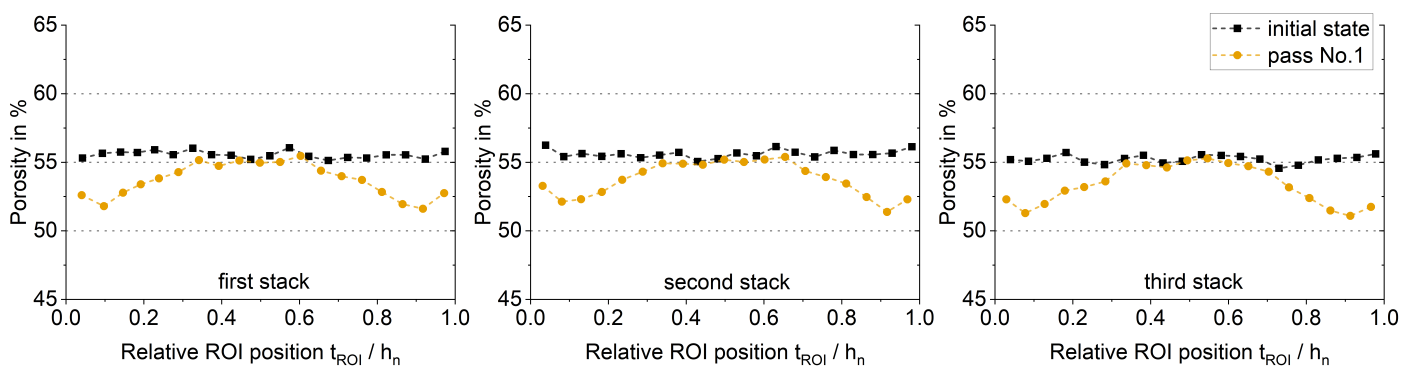


Figure A11. Series II: 20-0.05-1 ($l_d/h_m \approx 0.5$): Porosity change over relative sample depth (0 = upper surface; 0.5 = mid-section of sample; 1 = lower surface) due to rolling for first, second and third stack.

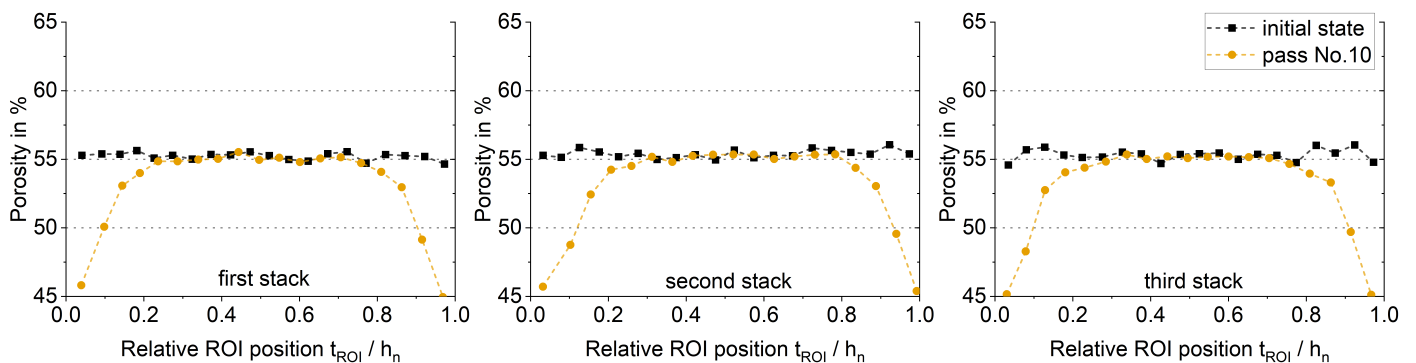


Figure A12. Series II: 20-0.05-10 ($l_d/h_m \approx 0.2$): Porosity change over relative sample depth (0 = upper surface; 0.5 = mid-section of sample; 1 = lower surface) due to rolling for first, second and third stack.

References

- Lippitz, N. Poröse Materialien zur Reduzierung von Hinterkantenschall an Flugzeugflügel. Ph.D. Thesis, Technische Universität Braunschweig, Braunschweig, Germany, 2017.
- Delfs, J.; Faßmann, B.; Lippitz, N.; Lummer, M.; Mößner, M.; Müller, L.; Rurkowska, K.; Uphoff, S. SFB 880: Aeroacoustic research for low noise take-off and landing. *CEAS Aeronaut. J.* **2014**, *5*, 403–417. [[CrossRef](#)]
- Delfs, J.W.; Appel, C.; Bernickey, P.; Blech, C.; Blinstrub, J.; Heykena, C.; Kumary, P.; Kutscherk, K.; Lippitz, N.; Lummer, M.; et al. Aircraft and technology for low noise short take-off and landing. In Proceedings of the 35th AIAA Applied Aerodynamics Conference, Denver, CO, USA, 5–9 June 2017. [[CrossRef](#)]
- Haines, M.M.; Stansfeld, S.A.; Job, R.; Berglund, B.; Head, J. Mental Health - A follow-up study of effects of chronic aircraft noise exposure on child stress responses and cognition. *Int. J. Epidemiol. Off. J. Int. Epidemiol. Assoc. IEA* **2001**, *30*, 839–845. [[CrossRef](#)]
- Haines, M.M.; Stansfeld, S.A.; Job, R.; Berglund, B.; Head, J. Chronic aircraft noise exposure, stress responses, mental health and cognitive performance in school children. *Psychol. Med. J. Res. Psychiatry Allied Sci.* **2001**, *31*, 265–278. [[CrossRef](#)] [[PubMed](#)]

6. Franssen, E.; Wiechen, C.; Nagelkerke, N.; Lebret, E. Aircraft noise around a large international airport and its impact on general health and medication use. *Occup. Environ. Med.* **2004**, *61*, 405–412. [[CrossRef](#)] [[PubMed](#)]
7. Faßmann, B.; Delfs, J.W.; Ewert, R.; Dierke, J. Reduction of emitted sound by application of porous trailing edges. In *SFB 880 - Fundamentals of High-Lift for Future Commercial Aircraft; Berichte aus der Luft- und Raumfahrttechnik*; Radespiel, R., Semaan, R., Eds.; TU Braunschweig Campus Forschungsflughafen: Braunschweig, Germany, 2013; pp. 1–12.
8. Fassmann, B.W.; Rautmann, C.; Ewert, R.; Delfs, J. Prediction of porous trailing edge noise reduction via acoustic perturbation equations and volume averaging. In *Proceedings of the 21st AIAA/CEAS Aeroacoustics Conference, Dallas, TX, USA, 22–26 June 2015*; p. 2525.
9. Vathylakis, A.; Chong, T.P.; Joseph, P.F. Poro-serrated trailing-edge devices for airfoil self-noise reduction. *AIAA J.* **2015**, *53*, 3379–3394. [[CrossRef](#)]
10. Alejandro, R.C.; Roberto, M.M.; Francesco, A.; Daniele, R.; Mirjam, S.; van der Sybrand, Z. Broadband Trailing-Edge Noise Reduction Using Permeable Metal Foams. In *Proceedings of the INTER-NOISE and NOISE-CON Congress and Conference Proceedings, Hong Kong, China, 27–30 August 2017; Volume 255*, pp. 2755–2765.
11. Allard, J.F.; Atalla, N. *Propagation of Sound in Porous Media: Modelling Sound Absorbing Materials*, 2nd ed.; Wiley: Hoboken, NJ, USA, 2009. [[CrossRef](#)]
12. Carpio, A.R.; Martínez, R.M.; Avallone, F.; Ragni, D.; Snellen, M.; Van Der Zwaag, S. Experimental characterization of the turbulent boundary layer over a porous trailing edge for noise abatement. *J. Sound Vib.* **2019**, *443*, 537–558. [[CrossRef](#)]
13. Showkat Ali, S.A.; Azarpeyvand, M.; Ilário da Silva, C.R. Trailing-edge flow and noise control using porous treatments. *J. Fluid Mech.* **2018**, *850*, 83–119. [[CrossRef](#)]
14. Lockard, D.P.; Lilley, G.M. The Airframe Noise Reduction Challenge. NASA/TM-2004-213013. 2004. Available online: <https://ntrs.nasa.gov/citations/20040065977> (accessed on 13 February 2023).
15. Mathew, J.; Singh, A.; Madsen, J.; Arce León, C. Serration Design Methodology for Wind Turbine Noise Reduction. *J. Physics: Conf. Ser.* **2016**, *753*, 022019. [[CrossRef](#)]
16. Tychsen, J.; Rösler, J. Production and characterization of porous materials with customized acoustic and mechanical properties. In *Notes on Numerical Fluid Mechanics and Multidisciplinary Design*; Springer: Berlin/Heidelberg, Germany, 2020.
17. Rossignol, K.S.; Suryadi, A.; Herr, M.; Schmidt, J.; Tychsen, J. Experimental investigation of porous materials for trailing-edge noise reduction. *Int. J. Aeroacoustics* **2020**, *19*, 365–384. [[CrossRef](#)]
18. Rossian, L.; Ewert, R.; Delfs, J. Advances in Numerical Simulation of Trailing Edge Noise Reduction by Porous Materials. In *SFB 880 - Fundamentals of High-Lift for Future Commercial Aircraft; Berichte aus der Luft- und Raumfahrttechnik*; Radespiel, R., Semaan, R., Eds.; TU Braunschweig Campus Forschungsflughafen: Braunschweig, Germany, 2017; pp. 1–10.
19. Rossian, L.; Ewert, R.; Delfs, J.W. Prediction of airfoil trailing edge noise reduction by application of complex porous material. In *Notes on Numerical Fluid Mechanics and Multidisciplinary Design*; Springer: Berlin/Heidelberg, Germany, 2018; Volume 136, pp. 647–657. [[CrossRef](#)]
20. Schulze, J.; Sesterhenn, J. Optimal distribution of porous media to reduce trailing edge noise. *Comput. Fluids* **2013**, *78*, 41–53. [[CrossRef](#)]
21. Tychsen, J.; Rösler, J. Production and characterization of experimental low noise trailing edges made of cold rolled porous aluminum with special attention to the influence of cold rolling on the mechanical stability of the investigated materials. *CEAS Aeronaut. J.* **2021**, *12*, 573–587. [[CrossRef](#)]
22. Hauger, A.; Muhr, T.; Kopp, R. Flexible rolling of tailor rolled blanks. *Stahl Eisen* **2006**, *126*, 21–23.
23. Deshpande, V.S.; Fleck, N.A. Isotropic constitutive models for metallic foams. *Journal of the Mechanics and Physics of Solids* **2000**, *48*, 1253–1283. [[CrossRef](#)]
24. Utsunomiya, H.; Matsumoto, R. Deformation Processes of Porous Metals and Metallic Foams (Review). *Procedia Mater. Sci.* **2014**, *4*, 245–249. [[CrossRef](#)]
25. Park, J.; Min, S.H.; Lee, W.H.; Park, N.S.; Kim, H.S.; Kim, J.O. Properties and filtration performance of microporous metal membranes fabricated by rolling process. *J. Water Reuse Desalin.* **2017**, *7*, 11–15. [[CrossRef](#)]
26. Shashikant, V.R.; Kanthale, V.S.; Kothavale, B.S. Review on Application of Aluminum Foam in Sound Absorption Technology. *Int. J. Curr. Eng. Technol.* **2011**, *4*, 178–181. [[CrossRef](#)]
27. Seuren, S.; Willkomm, J.; Bücker, M.; Bambach, M.; Hirt, G. Sensitivity analysis of a force and Microstructure model for plate rolling. In *Proceedings of the 14th International Conference on Metal Forming: Steel Research International*; Kusiak, J., Majta, J., Szeliga, D., Eds.; WILEY-VCH Verlag: Weinheim, Germany, 2012; pp. 91–94.
28. Seuren, S.; Seitz, J.; Krämer, A.; Bambach, M.; Hirt, G. Accounting for shear deformation in fast models for plate rolling. *Prod. Eng.* **2014**, *8*, 17–24. [[CrossRef](#)]
29. Mishin, O.V.; Bay, B.; Jensen, D.J. Through-thickness texture gradients in cold-rolled aluminum. *Metall. Mater. Trans. A* **2000**, *31*, 1653–1662. [[CrossRef](#)]
30. Mishin, O.V.; Bay, B.; Winther, G.; Jensen, D.J. The effect of roll gap geometry on microstructure in cold-rolled aluminum. *Acta Mater.* **2004**, *52*, 5761–5770. [[CrossRef](#)]
31. Tychsen, J.; Lippitz, N.; Rösler, J. Modification of porous aluminum by cold rolling for low-noise trailing edge applications. *Metals* **2018**, *8*, 598. [[CrossRef](#)]

32. Rossian, L. Minderung der Schallabstrahlung von aktiven Hochauftriebssystemen mit porösen Materialien. Ph.D. Thesis, Technischen Universität Carolo-Wilhelmina zu Braunschweig, Braunschweig, Germany, 2020.
33. Deutsches Institut für Normung. Prüfung Metallischer Werkstoffe—Druckversuch bei Raumtemperatur. Available online: <https://webstore.ansi.org/standards/din/din501062016de> (accessed on 23 November 2022).
34. Ashby, M.F. *Metal Foams: A Design Guide*; Butterworth-Heinemann: Boston, MA, USA, 2000.
35. DIN 862: Geometrical Product Specifications (GPS)-Callipers-Maximum Permissible Errors, 2015-03. Available online: <https://www.beuth.de/en/standard/din-862/145514621> (accessed on 23 November 2022).
36. Deutsches Institut für Normung. Acoustics; Materials for Acoustical Applications; Determination of Airflow Resistance German Version DIN EN 29053:1993-05. 1993. Available online: <https://www.beuth.de/en/standard/din-en-29053/2089412> (accessed on 17 June 2015).
37. Blech, C.; Appel, C.K.; Delfs, J.W.; Langer, S.C. Origin and prediction of cabin noise due to structure-borne sound. In *SFB 880 - Fundamentals of High-Lift for Future Commercial Aircraft; Berichte aus der Luft- und Raumfahrttechnik*; Radespiel, R., Semaan, R., Eds.; TU Braunschweig Campus Forschungsflughafen: Braunschweig, Germany, 2017; pp. 45–58.
38. Doroszko, M.; Seweryn, A. Pore-scale numerical modelling of large deformation behaviour of sintered porous metals under compression using computed microtomography. *Mech. Mater.* **2020**, *141*, 103259. [[CrossRef](#)]

Disclaimer/Publisher’s Note: The statements, opinions and data contained in all publications are solely those of the individual author(s) and contributor(s) and not of MDPI and/or the editor(s). MDPI and/or the editor(s) disclaim responsibility for any injury to people or property resulting from any ideas, methods, instructions or products referred to in the content.